

1 **Mesoscale Processes During the Genesis of Hurricane Karl (2010)**

2 Michael M. Bell*

3 *Colorado State University, Fort Collins, Colorado*

4 Michael T. Montgomery

5 *Department of Meteorology, Naval Postgraduate School, Monterey, California*

6 *Corresponding author address: Dept. of Atmospheric Science, 1371 Campus Delivery, Fort
7 Collins, Colorado 80523

8 E-mail: mmbell@colostate.edu

ABSTRACT

9 Observations from the PREDICT, GRIP, and IFEX field campaigns are an-
10 alyzed to investigate the mesoscale processes leading to tropical cyclogenesis
11 of Hurricane Karl (2010). Research aircraft missions provided Doppler radar,
12 in situ flight level, and dropsonde data documenting the structural changes of
13 the pre-depression disturbance. Following the pre-Karl wave pouch, varia-
14 tional analyses at the meso- β and meso- α scales suggest that the convective
15 cycle in Karl alternately built the low and mid-level circulations leading to
16 genesis episodically rather than through a sustained lowering of the convec-
17 tive mass flux from increased stabilization. Convective bursts that erupt in
18 the vorticity rich environment of the recirculating pouch region enhance the
19 low-level meso- β and meso- α scale circulation through vortex stretching. As
20 the convection wanes, the resulting stratiform precipitation strengthens the
21 mid-level circulation through convergence associated with ice microphysical
22 processes, protecting the disturbance from the intrusion of dry environmental
23 air. Once the column saturation fraction returns to a critical value, a subse-
24 quent convective burst below the mid-level circulation further enhances the
25 low-level circulation, and the convective cycle repeats. The analyses sug-
26 gest that the onset of deep convection and associated low-level spin-up were
27 closely related to the coupling of the vorticity and moisture fields at low and
28 mid-levels. Our interpretation of the observational analysis presented in this
29 study reaffirms a primary role of deep convection in the genesis process and
30 provides a hypothesis for the supporting role of stratiform precipitation and
31 the mid-level vortex.

³² **1. Introduction**

³³ An understanding of tropical storm formation requires insight into processes occurring at mul-
³⁴ tiple spatial and temporal scales. A synoptic-scale tropical wave can provide a protective environ-
³⁵ ment and background vorticity for a pre-depression, but does not guarantee that the pre-depression
³⁶ will intensify into a strong tropical cyclone (Frank 1970; Dunkerton et al. 2009). Processes on the
³⁷ meso- γ (\sim 2-20 km), meso- β (\sim 20 - 200 km), and meso- α (\sim 200 - 1000 km) scales within the
³⁸ pre-depression must concentrate enough planetary vorticity in the lower-troposphere to organize
³⁹ convection and sufficiently increase the rotational wind speeds to be declared a tropical depression
⁴⁰ or tropical storm. The processes by which this occurs are the primary focus of this paper.

⁴¹ While spontaneous tropical cyclone (TC) formation can occur in idealized numerical simulations
⁴² (e.g. Nolan et al. 2007), cyclogenesis in the real atmosphere occurs within a precursor synoptic-
⁴³ scale disturbance such as a tropical wave with favorable large-scale atmospheric and oceanic con-
⁴⁴ ditions (Gray 1968; McBride and Zehr 1981). A new model for cyclogenesis in tropical waves
⁴⁵ developed by Dunkerton et al. (2009, hereafter DMW09) describes a recirculation region within
⁴⁶ the critical layer of the parent wave where air tends to be repeatedly moistened by cumulus con-
⁴⁷ vection, protected to some degree from lateral intrusion of dry air and deformation by horizontal
⁴⁸ or vertical shear, and (thanks to its location near the critical level) able to keep pace with the parent
⁴⁹ wave until the dominant vortex has strengthened into a self-maintaining entity. The combination
⁵⁰ of the associated genesis sequence and the overarching framework for describing how such hybrid
⁵¹ wave-vortex structures become tropical depressions is likened to the development of a marsupial
⁵² infant in its mother's pouch (see DMW09, Montgomery et al. 2010; Wang et al. 2010a,b).

⁵³ In late summer 2010 the Pre-Depression Investigation of Cloud Systems in the Tropics (PRE-
⁵⁴ DICT) field campaign was conducted to improve our understanding of how tropical waves transi-

55 tion into tropical cyclones and test the principal hypothesis that tropical storm formation is greatly
56 favored in the critical-layer region of the synoptic-scale pre-depression disturbance (Montgomery
57 et al. 2012). The National Science Foundation (NSF) supported the PREDICT field campaign,
58 which involved 25 research flights into Atlantic tropical disturbances. The PREDICT campaign
59 was conducted in conjunction with NASA Genesis and Rapid Intensification Processes (GRIP)
60 and National Oceanic and Atmospheric Administration (NOAA) Intensity Forecast Experiment
61 (IFEX) campaigns.

62 Composite analyses of developing and non-developing disturbances (hereafter, ‘developers’ and
63 ‘non-developers’) using the PREDICT dataset have revealed distinctions between favorable and
64 unfavorable thermodynamic environments for genesis. Montgomery and Smith (2012), Davis and
65 Ahijevych (2013), and Komaromi (2012) showed that development depends strongly on available
66 moisture above the boundary layer. Developers had higher equivalent potential temperature (θ_e)
67 in the low to mid-troposphere due to both warmer and moister air, while non-developers had high
68 convective available potential energy (CAPE) relative to the developers due to cooler and drier
69 air at mid-levels. In particular, Smith and Montgomery (2012) found that “the most prominent
70 difference between the non-developing system (ex-Gaston, our insertion) and the two developing
71 systems (pre-Karl and pre-Matthew, our insertion) was the much larger reduction of θ_e between
72 the surface and a height of 3 km, typically 25 K in the non-developing system, compared with
73 only 17 K in the developing systems. Conventional wisdom would suggest that, for this reason,
74 the convective downdrafts would be stronger in the non-developing system and would thereby act
75 to suppress the development.”

76 Smith and Montgomery (2012) proposed an alternative hypothesis “in which the drier air weak-
77 ens the convective updrafts and thereby the convective amplification of absolute vorticity necessary
78 for development.” This alternative hypothesis was tested by Freismuth et al. (2016) for the non-

79 developing case of ex-Gaston using large-scale analyses. Freismuth et al. showed that “entrained,
80 dry air near 600 hPa thwarted convective updrafts and vertical mass flux, which in turn led to a
81 reduction in vorticity and a compromised pouch at these middle levels. A compromised pouch
82 allows further intrusion of dry air and quenching of subsequent convection, therefore hindering
83 vorticity amplification through vortex tube stretching.” Gjorgjevska and Raymond (2014) argued
84 that a reduction in mid-level vorticity may have occurred prior to the ingestion of dry air, which
85 initially weakened the pouch and allowed for subsequent intrusion of dry air. The findings of both
86 Freismuth et al. (2016) and Gjorgjevska and Raymond (2014) point to a potentially important
87 positive role of the middle-level cyclonic circulation by providing protection against dry-air intru-
88 sions from the complex environment and supporting a favorable region for persistent convective
89 activity and vortex-tube stretching on the system scale circulation.

90 Numerical simulations and large-scale analyses by Montgomery et al. (2010), Wang et al.
91 (2010a, 2012), Wang (2012) and others have now provided abundant evidence that a deep, moist
92 pouch is a necessary condition for the development of a tropical disturbance in the Atlantic basin,
93 but the specific role of the mid-level and low-level circulations, enhanced temperature and mois-
94 ture at mid-levels, and the relative importance of deep, congestus, and stratiform convection in the
95 development process are still under debate. As an example of the diversity of thought on the key
96 ingredients of the genesis process, a competing theory on the role of the middle-level circulation
97 has been proposed by D. Raymond and co-workers. The idea is that the enhanced static stabil-
98 ity associated with a mid-level cyclonic vortex is an essential element of developers (Raymond
99 and Sessions 2007; Raymond et al. 2011; Raymond 2012; Davis and Ahijevych 2013; Zawislak
100 and Zipser 2014; Gjorgjevska and Raymond 2014). This theory emphasizes the thermodynamic
101 structure of the tropical disturbance, revising an early emphasis on stratiform mesoscale convec-
102 tive systems (MCSs) that emerged from prior field campaigns two decades earlier (e.g. Bister and

¹⁰³ Emanuel 1997; Raymond et al. 1998; Simpson et al. 1997). The work of Raymond et al. (2011)
¹⁰⁴ and Gjorgjevska and Raymond (2014) has proposed a refinement of the marsupial paradigm, sug-
¹⁰⁵ gesting that the enhanced stability causes a lowering of the convective mass flux and, by mass
¹⁰⁶ continuity, a spin up of the lower troposphere by the convergence of cyclonic vertical vorticity
¹⁰⁷ from the near environment. In the proposed refinement, the thermodynamic structure that is in
¹⁰⁸ balance with the vorticity provides a strong control on the humidity profile and convective mass
¹⁰⁹ flux through a “moisture quasi-equilibrium” process (Raymond and Flores 2017).

¹¹⁰ Organized deep convection has been acknowledged as a necessary component of genesis for
¹¹¹ several decades (e.g. Gray 1968; Houze et al. 2009), and is in fact part of the definition of a TC
¹¹² according to the National Hurricane Center (see <http://www.nhc.noaa.gov/aboutgloss.shtml>). Ob-
¹¹³ servations suggest repeated bursts of vortical deep convection are an important component of the
¹¹⁴ genesis process (Zehr 1992; Gjorgjevska and Raymond 2014; Raymond et al. 1998). A key cloud
¹¹⁵ scale process identified by numerical studies (Hendricks et al. 2004; Montgomery et al. 2006;
¹¹⁶ Nguyen et al. 2008; Zhang et al. 2011) is that low-level convergence driven by deep convection
¹¹⁷ in a rotating environment amplifies pre-existing vertical vorticity locally by vortex tube stretch-
¹¹⁸ ing, and that the amplified vorticity outlives the deep convection that produced it. Wissmeier and
¹¹⁹ Smith (2011) and Kilroy and Smith (2012) showed that vertical vorticity could be amplified by
¹²⁰ an order of magnitude by even moderate, short-lived convective updrafts in idealized numerical
¹²¹ simulations of tropical convection. Vortical remnants concentrated by deep convection will tend
¹²² to aggregate within the broader cyclonic circulation, leading to a corresponding upscale vorticity
¹²³ and energy cascade and further amplification of vertical vorticity by subsequent convective bursts.
¹²⁴ The system-scale inflow forced by the aggregate latent heating from the convective elements leads
¹²⁵ to an inward advection of convectively enhanced vorticity. Stokes’ theorem applied to a fixed area

¹²⁶ surrounding the convection implies that there will be an accompanying increase in the strength of
¹²⁷ the disturbance-scale circulation on account of the import of ambient absolute vorticity.

¹²⁸ Observations have shown evidence for the presence of vortical deep convection in several TC
¹²⁹ genesis cases. Zipser and Gautier (1978) concluded that a giant updraft within an MCS accounted
¹³⁰ for the majority of upward mass flux in a tropical depression off the coast of Africa in 1974,
¹³¹ and that the low-level convergence supporting the MCS could stretch the environmental vorticity
¹³² at a rate that would account for much of the intensification of the depression. Further evidence
¹³³ showing the existence and operation of vortical deep convection has been found since those early
¹³⁴ observations (Reasor et al. 2005; Sippel et al. 2006; Houze et al. 2009; Bell and Montgomery
¹³⁵ 2010; Sanger et al. 2013). However, most of these observations consist of snapshots or short
¹³⁶ time samples, and it has been difficult using observations only to piece together the cumulative
¹³⁷ effects of deep convection in the pre-genesis period. The comprehensive dataset obtained in pre-
¹³⁸ depression Karl (2010) provides a unique series of aircraft observations to help investigate the
¹³⁹ roles of convective and stratiform precipitation processes in TC genesis.

¹⁴⁰ Observations from pre-depression Karl collected during PREDICT have been used in this study
¹⁴¹ to quantify the dynamic and thermodynamic effects of deep convection, stratiform precipitation,
¹⁴² and vortex intensification following the recirculating pouch region for five days leading up to gen-
¹⁴³ esis. Doppler radar, in situ, and dropsonde observations have been analyzed using a spline-based
¹⁴⁴ variational technique called SAMURAI (Bell et al. 2012) to examine the mesoscale structure.
¹⁴⁵ Similar to the results reported by Lussier et al. (2014), circulation tendencies suggest progres-
¹⁴⁶ sive development of the low-level circulation through low-level convergence of vorticity in deep
¹⁴⁷ convective bursts. A strong mid-level circulation develops also over this period, consistent with
¹⁴⁸ the hypothesis that stratiform precipitation processes also play an important role in genesis. Our

¹⁴⁹ results will suggest that divergence profiles associated with convectively inactive MCS regions in
¹⁵⁰ pre-depression Karl contributed to a low-level spin-down of the vortex.

¹⁵¹ We propose here the hypothesis that the primary role of stratiform MCS regions is to promote
¹⁵² mid-level convergence that enhances the mid-level meso- α scale pouch circulation. As anticipated
¹⁵³ by the foregoing discussions, the enhanced mid-level pouch region serves to recirculate moisture
¹⁵⁴ above the boundary layer in a frame of reference moving with the synoptic-scale disturbance.
¹⁵⁵ The enhanced moisture leads to decreased entrainment for subsequent bursts of deep convection
¹⁵⁶ (Holloway and Neelin 2009; James and Markowski 2010; Kilroy and Smith 2012) that can spin-up
¹⁵⁷ the low-level circulation. This hypothesis is distinct from the emphasis in previous studies on the
¹⁵⁸ importance of the enhanced static stability leading to genesis. Our results suggest that the low-
¹⁵⁹ level cooling seen in previous composite analyses is episodic rather than persistent, and that the
¹⁶⁰ upper-level warming is associated with the developing warm-cored vortex.

¹⁶¹ In addition to the dynamic effect of enhancing the mid-level pouch, the direct effect of low-
¹⁶² level moistening and cooling by stratiform rain from MCS regions is also beneficial, and may
¹⁶³ help the recovery of the low-level relative humidity after bursts of deep convection. A positive
¹⁶⁴ phasing between the low-level cooling and the diurnal cycle appears to have also contributed to
¹⁶⁵ Karl's genesis, consistent with the numerical study of Melhauser and Zhang (2014). Our analysis
¹⁶⁶ suggests that a critical value of saturation fraction for the layer below 700-hPa near 85% relative
¹⁶⁷ humidity (RH) allows for the onset of deep convection, similar to that analyzed in large-scale
¹⁶⁸ tropical convection (Neelin et al. 2009). The episodic nature of the convective bursts is tied closely
¹⁶⁹ to moisture availability above the boundary layer, consistent with the hypothesis of Holloway and
¹⁷⁰ Neelin (2009) that the deep convective onset is due to enhanced buoyancy of an entraining air
¹⁷¹ parcel. The saturation fraction below 700 hPa stays close to 85% in the days leading up to genesis,

¹⁷² with repeated bursts of deep convection occurring when the meso- α scale environment exceeds
¹⁷³ this critical value, resulting in strong low-level convergence and spin-up of the TC.

¹⁷⁴ An outline of the remaining paper is as follows: Section 2 describes the PREDICT dataset
¹⁷⁵ and the analysis methodology used in this study. Results from the mesoscale analysis of Karl's
¹⁷⁶ genesis are presented in Section 3. The circulation dynamics of the developing tropical cyclone
¹⁷⁷ are presented in Section 4. Section 5 summarizes the results and discusses their implications in
¹⁷⁸ the context of recent studies.

¹⁷⁹ 2. Data and Methodology

¹⁸⁰ The NSF/National Center for Atmospheric Research (NCAR) Gulfstream-V (GV) aircraft col-
¹⁸¹ lected high-altitude (\sim 13-14 km) in situ and full-tropospheric dropsonde observations in a meso- α
¹⁸² scale region encompassing the pouch and its nearby environment. GV in situ and dropsonde data
¹⁸³ were processed and quality controlled by the NCAR Earth Observing Laboratory. A correction for
¹⁸⁴ a dry bias in the relative humidity for dropsondes from 2010 was applied. Two NOAA WP-3Ds
¹⁸⁵ (P3s) were available for three missions that collected low-altitude (\sim 3 km) in situ and dropsonde
¹⁸⁶ observations, and added Doppler radar observations. The X-band (3-cm) wavelength tail Doppler
¹⁸⁷ radar aboard the P3 aircraft employed a fore/aft scanning technique that provided radial velocity
¹⁸⁸ data in a cone $\sim 20^\circ$ from the track both fore and aft of the aircraft. Three-dimensional winds and
¹⁸⁹ precipitation structure were derived from the multiple Doppler velocities. Following the method-
¹⁹⁰ ology developed by Bosart et al. (2002), the data were first corrected for navigational errors and
¹⁹¹ manually edited to remove ocean returns, radar sidelobes, and other artifacts. The Doppler radar
¹⁹² data was the only available tool to probe the three-dimensional convective structure of the pouch
¹⁹³ on the meso- γ and meso- β scales (Marks and Houze 1987; Reasor et al. 2005), but was only
¹⁹⁴ available around 0000 and 1200 UTC on 13 September and 0000 UTC on 14 September. Limited

195 radar echoes during the 0000 UTC 14 September P-3 mission precluded quantitative analysis of
196 the convective structure at that time, therefore the radar analysis presented herein focuses on 13
197 September.

198 The SAMURAI variational analysis package (Bell et al. 2012; Foerster et al. 2014; Lussier et al.
199 2014; Foerster and Bell 2017) was used to composite the research observations at horizontal node
200 spacings of 25 km and 2 km to examine the pre-depression structure at meso- α and meso- β scales,
201 respectively. One of the advantages of variational analyses such as SAMURAI is the capability to
202 combine observations from different instruments with a prior estimate of the atmospheric state. For
203 this study, the 0.25 degree European Center for Medium Range Weather Forecasting (ECMWF)
204 analyses were used as an initial estimate for the 25 km Cartesian grid analyses. The SAMURAI
205 meso- α scale analyses were then calculated using dropsondes and satellite derived atmospheric
206 motion vectors (Velden et al. 2005) in a six hour window around the mission on each analysis day.
207 An isotropic, Gaussian background error covariance was used with the error standard deviations
208 shown in Table 1. The ECMWF analyses were found to have a reasonably good agreement with
209 the observations at the meso- α scale, such that the analyses were not overly sensitive to the pre-
210 scribed error magnitudes. The Gaussian covariance length scale was set to $4\Delta x$ in the horizontal
211 to focus on the primary scales resolvable at each nodal resolution. The vertical grid spacing was
212 chosen to be 500 m for all composites, with a $2\Delta z$ vertical covariance length scale. A conjugate
213 gradient algorithm was used to minimize an incremental form of the variational cost function with
214 a mass continuity constraint. No other balance or physical constraints were used in the cost func-
215 tion minimization. A background vertical velocity error standard deviation of 1 m s^{-1} constrains
216 the divergence through the mass continuity constraint to be representative of hydrostatic vertical
217 motions.

218 The 25 km SAMURAI analyses were then used as an initial estimate for the 2 km analyses,
 219 and the data window was reduced to \sim 15 minutes. The 2 km nodal spacing was chosen to ap-
 220 proximately match the along-track resolution of the NOAA P-3 tail Doppler radar observations.
 221 Dropsondes and satellite-derived wind vectors were also included in the meso- β scale analyses to
 222 allow finer spatial scale information to be retrieved from those data, but the wind field was pri-
 223 marily determined from Doppler radar observations. As shown in Table 1, the background error
 224 standard deviation was increased to 25 m s^{-1} for all three wind components in the 2 km analyses.
 225 The large background error essentially makes the meso- β scale analyses independent of the initial
 226 estimate where Doppler radar observations were available. Given the poor spatial sampling at this
 227 scale from the dropsonde data alone, the analyzed winds were removed in areas with no radar
 228 reflectivity.

229 As a quantitative tool for examining the nature of Karl's spin up, the circulation equation was
 230 used to calculate the contributions to changes in circulation during the pre-genesis period from
 231 the SAMURAI analyses. The form of the equation used in this study was derived by Davis and
 232 Galarneau (2009) and is given by:

$$\frac{\partial C}{\partial t} = -\bar{\eta}\tilde{\delta}A - \oint \eta' \mathbf{v}' \cdot \hat{\mathbf{n}} dl + \oint \bar{\omega} \left(\hat{\mathbf{k}} \times \frac{\partial \mathbf{V}}{\partial p} \right) \cdot \hat{\mathbf{n}} dl + \oint (\hat{\mathbf{k}} \times \mathbf{F}) \cdot \hat{\mathbf{n}} dl \quad (1)$$

233 where C denotes circulation, t denotes time, η denotes absolute vorticity, δ denotes divergence,
 234 and A denotes the area of the domain. Overbars represent averaging around the perimeter, primes
 235 represent perturbations from the perimeter average, and the tilde represents areal averaging. Addi-
 236 tional symbols denote the vertical velocity in pressure coordinates ω , the perturbation \mathbf{v}' and total
 237 \mathbf{V} horizontal vector winds, friction and sub-grid scale forces \mathbf{F} , unit vectors in the normal $\hat{\mathbf{n}}$ and
 238 vertical directions $\hat{\mathbf{k}}$, and perimeter length increment dl .

239 This form of the circulation equation results from integrating the flux form of the vertical vor-
240 ticity equation (Haynes and McIntyre 1987) and decomposing the stretching term into mean and
241 eddy components. As is evident from Eq. (1), the four contributions to the circulation tendency
242 are from the area-averaged horizontal convergence of perimeter-averaged absolute vorticity, eddy
243 fluxes of vorticity at the perimeter, tilting contributions at the perimeter, and Reynolds stress at the
244 perimeter, respectively. As pointed out by Davis and Galarneau (2009), the separation of the first
245 two terms into mean horizontal convergence and eddy fluxes allows for a more straight-forward
246 interpretation of contributions from vortex stretching and horizontal advection, respectively. Fric-
247 tion was estimated following the method described in Raymond and Lopez-Carillo (2011), using a
248 bulk aerodynamic formula for surface stress that decayed exponentially over a scale height of 1.25
249 km. Due to the extended length of time between flights, it is not possible to calculate the actual
250 circulation tendency on the left hand side of Eq. (1) with sufficient accuracy from the observations,
251 but the circulation budget obtained from the summation of the right hand side allows for insight
252 into the leading order processes that contribute to vortex spin-up.

253 **3. PREDICT Analysis**

254 *a. Time-series analysis*

255 Figure 1a shows the track of pre-Karl from PREDICT research missions (thick blue line) and
256 Karl after it was declared by the National Hurricane Center (NHC) (best track, thin black line).
257 The red stars denote the sweet spot location at 850 hPa deduced from the SAMURAI analyses
258 of each mission data. The sweet spot is defined by the intersection of the critical latitude (where
259 the zonal flow is equal to the wave phase speed) and the wave trough axis (where the meridional
260 velocity is zero). The SAMURAI analyses were first performed in a co-moving frame following

261 the estimated motion of the pre-depression disturbance from ECMWF analyses. A linear fit of the
262 analyzed positions (thick blue line) was used to derive an average system translation speed for the
263 final SAMURAI analyses (red stars). The analyses shown in the next section are centered on the
264 linear track, but the sweet spot location varies somewhat from mission to mission.

265 Previous work has typically divided the genesis and further intensification into a series of stages,
266 ranging from a pre-conditioning phase, genesis phase, and more mature phases of the tropical cy-
267 clone lifecycle. While these may be useful for delineating the morphological stages in a cyclone's
268 evolution, we note that there is no formal, universally accepted definition for tropical cyclogenesis,
269 but rather a somewhat subjective designation within a continuum of intensifying states that meet
270 certain thresholds of convective organization and wind speed. In this study, we use the operational
271 designation of tropical storm status by NHC to define Karl's genesis time, but a precise definition
272 of genesis will be sidestepped in order to focus on understanding the formation process.

273 The NHC best track for Karl began on late 13 September, denoted by the 'L' which was approx-
274 imately 2 degrees south of the co-moving center. The best track, which uses earth-relative winds,
275 moved northward over the following day prior to tropical depression (denoted 'Lx') and tropical
276 storm designation (denoted by the open hurricane symbol). The genesis location, as marked by the
277 tropical storm designation, is closely located near the pouch sweet spot at 1800 UTC 14 Septem-
278 ber. Karl continued to move westward as it developed into a hurricane, and was subsequently
279 sampled by IFEX and GRIP research missions (gray stars).

280 Figure 1 shows also the infrared satellite imagery coincident with some of the aircraft missions
281 leading up to genesis. During the first GV aircraft mission at 1200 UTC 10 September (Fig. 1e),
282 the cloud cluster was relatively disorganized and composed mostly of cloud tops warmer than -70
283 °C (denoted in green and blue) associated with stratiform MCSs. At 0000 UTC 13 September
284 (Fig. 1d), there were isolated regions of deep convection (<-70 °C cloud tops denoted in red and

yellow) interspersed with warmer cloud tops near the sweet spot. At 1200 UTC later that same day (Fig. 1c), there was a north-south elongated region of active deep convection from 15 to 19 deg N, with a broader region of convective activity well to the south of the sweet spot. This 12-hr period is examined in greater detail below. Well-organized deep convection with some banding was evident by 1800 UTC 14 September at the time of genesis (Fig. 1b).

Figure 2 shows a time series of the analyzed meso- α circulation at 850 and 500 hPa over a 600 x 600 km domain (Fig. 2a), a 200 x 200 km domain (Fig. 2b), and areal fraction of cold-cloud tops from Davis and Ahijevych (2012) (black line). The cold-cloud fraction (CCF) below -60° C was calculated within 200 km of the model-consensus circulation center, corresponding roughly to the meso- α analysis domain. There was almost no 500 hPa circulation (Fig. 2a, blue triangles) above the 850 hPa circulation (red circles) at 1200 UTC 10 September on the larger meso- α domain. The weak mid-level circulation may be due in part to misalignment of the vortex in the vertical, such that the mid-level circulation was not fully within the analysis domain. A brief intensification of the 850 hPa circulation was seen after the first aircraft mission that was followed by a slow decline over the next several days.

The peaks in cold-cloud fraction (CCF) represent the time of deep convective bursts, showing the episodic nature of the convection. The aircraft sampled the pre-depression after a strong convective burst the morning of 11 September when extensive stratiform precipitation was evident in satellite imagery (not shown) and there was a marked increase in 500 hPa circulation analyzed at 1800 UTC 11 September (see Fig. 2). The other periods where the CCF is declining in the time series are generally associated with the convective to stratiform transition.

The linear interpolation of circulation between aircraft missions on 10 and 11 September most likely obscures a more complex time series than depicted. We speculate that the 850 hPa circulation spun-down prior to the convective burst, but was followed by some spin-up when the deep

309 convection erupted. The net result over this period was a slight weakening of the 850 hPa circu-
310 lation. A steady, alternating intensification of both the 850 and 500 hPa circulations followed as
311 the series of convective bursts continued. Genesis declaration by NHC corresponds to the time
312 when the average absolute vorticity in the larger domain exceeded $8 \times 10^{-5} \text{ s}^{-1}$ at both the low
313 and mid-levels.

314 The smaller 200 x 200 km domain (Fig. 2b) shows larger amplitude fluctuations in the circula-
315 tion over time than in the larger domain. Like the larger domain, the initial circulation at 500 hPa
316 was weak but increased significantly as the first convective burst decayed, but the decrease in 850
317 hPa circulation over the first 18 hours is more evident in the smaller domain. The 850 and 500 hPa
318 circulations changes are more clearly out of phase on this domain, with the increase at one level
319 occurring at the same time as a decrease in the other level. The circulation increases at 850 hPa
320 tend to occur at the peak of the cold-cloud fraction during the convective bursts, followed by in-
321 creases at 500 hPa during the stratiform transition period. In the upcoming Section 4 a circulation
322 analysis is presented that provides more detail on the circulation changes over the multiple day
323 period leading up to genesis.

324 *b. Meso- α and meso- β scale structure*

325 The 25-km SAMURAI analyses for all missions have been performed, but here we focus on
326 the analysis at 00 and 12 UTC on 13 September since a) this was the only day that quality radar
327 data was available to provide a more detailed look at the meso- β scale structure to accompany the
328 meso- α scale analysis, and b) we believe the 12-hour evolution on this day is representative of
329 the processes occurring during the predominately convective and stratiform periods at other times.
330 Figure 3 shows the low-level SAMURAI analysis of the meso- α and meso- β scale kinematic,
331 moisture, and reflectivity at 00 UTC 13 September. For the purposes of this paper, we define “low-

332 levels” to be below 700 hPa or 3 km altitude, “mid-levels” to be between 700 hPa and 400 hPa,
333 or 3 - 8 km altitude, and “upper-levels” to be above 400 hPa or 8 km. To compare with previous
334 studies and simplify the interpretation of the circulation dynamics, the meso- α scale analyses were
335 output on constant pressure levels, with the 850 and 500 hPa levels highlighted here. Meso- β scale
336 analyses were composed primarily of Doppler radar data that was more appropriate to analyze on
337 constant height levels at approximately the same altitudes of 1.5 and 6 km, respectively.

338 The analyzed wind in the co-moving frame of reference (black vectors) indicates a broad cy-
339 clonic recirculating flow on the meso- α scale (25 km nodal mesh) centered around the sweet spot
340 (red star). The red vectors indicate the dropsonde wind observations used in the analysis in the
341 co-moving frame. The strongest winds at 850 hPa exceed $\sim 9 \text{ m s}^{-1}$ in the co-moving frame of
342 reference and are found $\sim 125 \text{ km}$ south-southeast of the sweet spot. The analyzed flow field is
343 in good overall agreement with the observations, with the exception of a few instances. Recall
344 that the analyzed fields incorporate the global model background estimate, observation errors, and
345 mass continuity constraints. For example, 50 km west and 125 km north of the sweet spot, denoted
346 here as (-50, 125), the dropsonde wind is northeasterly while the analyzed wind is northwesterly.
347 The northeasterly wind would imply strong convergence in the presence of the northwesterly flow
348 indicated by the other nearby dropsondes, and is likely not representative of the meso- α scale flow.

349 Figure 3a shows absolute vertical vorticity on the meso- α scale with filled color contours. A
350 SW-NE elongated region of positive absolute vorticity had an enhanced central core approximately
351 200 km across centered around the sweet spot (red star). Six negative absolute vorticity regions
352 were found on the periphery of the enhanced cyclonic region 125 - 250 km away from the sweet
353 spot. The central core of enhanced cyclonic vorticity was greater than approximately three times
354 the planetary vorticity at this latitude.

355 The thick white contours in Fig. 3a indicate relative humidity (RH) contoured in 10% intervals.
356 A broad region of RH above 75% was co-located with the recirculating flow. RH exceeded 85% in
357 the higher vorticity region near the sweet spot. The moist pouch center above the boundary layer
358 is consistent with the hypothesis that recirculating air parcels within the disturbance are repeatedly
359 moistened by convective activity as the pre-depression moved westward.

360 The dashed yellow box in Fig. 3a indicates the meso- β scale analysis region in Fig. 3b where
361 Doppler radar observations were collected by the NOAA P3 aircraft. Throughout most of the
362 domain the winds were from the north, but on the southern end of the domain the winds turned cy-
363 clonically to the southeast. The winds derived from the Doppler radar are in good agreement with
364 the meso- α scale winds analyzed from the dropsondes and the global analysis. The thick black
365 contours denote isopleths of absolute vorticity. The vorticity in the northern half was comprised
366 primarily of shear vorticity, while the vorticity in the southern half was comprised primarily of
367 curvature vorticity.

368 A higher level of detail is apparent in the meso- β vorticity field in comparison to the meso- α
369 analysis. A SW-NE elongated region of vorticity anomalies is evident in the northern half of the
370 analysis domain. There is a strong cyclonic vorticity maximum at (-55, 10) with a value exceeding
371 $2 \times 10^{-4} \text{ s}^{-1}$. Adjacent to this cyclonic region are two anticyclonic vorticity regions with maximum
372 values lower than $-1 \times 10^{-4} \text{ s}^{-1}$ and $-2 \times 10^{-4} \text{ s}^{-1}$, respectively. In the southern half of the analysis
373 domain there is an E-W elongated region of cyclonic vorticity approximately 70 km in length.

374 The radar reflectivity is shown in Fig. 3b with filled color contours. A broad region of stratiform
375 precipitation below 35 dBZ covers most of the analysis domain, punctuated by two convective
376 cores near (-70, -15) and (-60, 5). The latter convective core was deeper, and appears to be associ-
377 ated with the -70°C cold cloud top region in the center of Fig. 1d. Satellite animations suggest the
378 convective core was decaying at this time (not shown). The deeper convective core was co-located

379 with one of the strong cyclonic vorticity anomalies. To the northeast of these two cores was a
380 region of moderate stratiform rain co-located with a stronger anticyclonic vorticity anomaly. An-
381 other region of moderate stratiform rain was co-located with the cyclonic curvature in the southern
382 portion of the domain.

383 Figure 4 shows the 500 hPa and 6 km altitude SAMURAI analyses in similar format to Figure 3.
384 The recirculating flow is stronger at 6 km than at 1.5 km, with the local circulation center displaced
385 ~225 km to the southwest of the 1.5 km altitude sweet spot. The separation of the circulation
386 centers at low and mid-levels was likely due to vertical shearing flow of 4 m s^{-1} from 925 to 500
387 hPa at this time (Davis and Ahijevych 2012, c.f. Fig. 10). The recirculating flow was elongated in
388 the N-S direction, and the absolute vertical vorticity field (color) was also elongated largely in the
389 N-S direction, with two trailing vorticity bands extending NNE and SSW from a central vorticity
390 maximum that exceeds $3 \times 10^{-4} \text{ s}^{-1}$. The central vorticity core is bordered by regions of negative
391 relative vorticity, but unlike 1.5 km altitude there is no negative absolute vorticity.

392 The RH field (white contours) was closely aligned with the recirculating flow field and absolute
393 vorticity in the SW-NE direction. A region over 600 km long in the N-S direction where the RH
394 exceeded 85% was found near the central vorticity core. The central region that was well-sampled
395 by the dropsondes shows peak RH values exceeded 95%. A strong moisture gradient was evident
396 in the E-W direction, with RH below 65% to the SE and below 35% to the NW of the mid-level
397 vorticity core. The close coupling of enhanced positive vorticity associated with recirculating flow
398 in the translating reference frame and enhanced moisture within this region provide observational
399 evidence of the protection from dry environmental air within the marsupial pouch at mid-levels.

400 Figure 4b shows the Doppler radar analysis for the dashed box region in Figure 3a. The broad
401 recirculation region present on the meso- α scale is evident also on the meso- β scale. At a more
402 detailed level however, there are some distinct differences. The meso- β scale circulation center

403 was located 75 km north of the derived meso- α scale circulation center. Stronger northerly winds
404 around 15 m s^{-1} are found to the W of the center, with weak westerlies S of the center in the
405 co-moving frame.

406 The vorticity field on the meso- β scale depicts a broad region of positive vorticity associated
407 with both curvature and shear contributions, with two distinct maxima near (-40, -50) and (-40,
408 10). The northern maximum exceeded $9 \times 10^{-4} \text{ s}^{-1}$ and was part of an asymmetric vorticity dipole
409 with a corresponding weaker region of negative vorticity to the west that was about $-1 \times 10^{-4} \text{ s}^{-1}$.
410 The southern maximum exceeded $1.5 \times 10^{-3} \text{ s}^{-1}$ and was co-located with the meso- β circulation
411 center. The southern maximum was approximately 40 km across, which is less than two nodes in
412 the meso- α scale analysis. Based on the available data it is unclear whether the meso- β center is
413 representative of a distinct circulation or is just a more resolved depiction of the circulation evident
414 on the meso- α scale.

415 With a stronger suggestion of curved banding in the reflectivity field at 6 km altitude compared
416 to 1.5 km, the reflectivity structure appears to be more congruent with the horizontal winds at 6 km.
417 The decaying convective core discussed in Fig. 3b was approximately centered on the northern
418 asymmetric vorticity dipole. The southern vorticity maximum was co-located with a region of
419 weaker stratiform precipitation.

420 Twelve hours later, the kinematics, thermodynamics, and precipitation share many similar char-
421 acteristics with the 0000 UTC structure, but with some important changes relevant to the genesis
422 process. The vorticity increased throughout the meso- α scale domain at 850 hPa (Fig. 5a), with
423 almost no negative absolute vorticity apparent near the sweet spot. RH increased also, with a
424 broader region exceeding 85% and a smaller region exceeding 95% that was co-located with the
425 highest vorticity maximum.

426 Coincident with the increase in vorticity and RH on the meso- α scale was a change in the vor-
427 ticity and convective character on the meso- β scale (Fig. 5b). Higher concentrations of positive
428 vorticity were co-located with enhanced reflectivity in convective cores. In contrast to the pre-
429 dominately stratiform precipitation pattern seen at 0000 UTC, the reflectivity had a more cellular
430 appearance and was generally stronger throughout the analysis domain. The significant outbreak
431 of deep convection apparent in the satellite imagery (Fig. 1c) occurred very close to the sweet
432 spot, which provided higher background vorticity for low-level vortex stretching in the convective
433 cores. The peak vorticity value at 1.5 km exceeded $9 \times 10^{-4} \text{ s}^{-1}$ and was nearly twice as high as
434 the observed values at 0000 UTC.

435 At 6 km altitude however, the peak vorticity on the meso- α scale has decreased by nearly one
436 half over this 12-hour period (Fig. 6a). The elongated vorticity and RH region is more compact
437 in the N-S direction, with the 85% RH region reduced to 550 km in length. The strong E-W
438 moisture gradient is still evident. On the meso- β scale (Fig. 6b), the cellular convective cores are
439 still apparent at 6 km altitude, and are generally associated with strong vorticity dipoles. Broad
440 recirculating flow is still evident at this scale, but the detailed wind and vorticity fields at 6 km are
441 more influenced by the convective activity and tilting of horizontal vorticity associated with local
442 vertical wind shear (c.f. Bell and Montgomery 2010).

443 *c. Convective and stratiform contributions to genesis*

444 The SAMURAI analysis at 0000 and 1200 UTC suggests a shift from predominately stratiform
445 to predominately deep convective activity on 13 September that has profound implications for
446 vortex development at these times. The vertical divergence profile of these two precipitation types
447 results in positive and negative vortex stretching at different altitudes that modify the circulation.

⁴⁴⁸ Vertical cross-sections through the meso- β scale analysis in Fig. 7 show representative examples
⁴⁴⁹ of the convection and vorticity that illustrate their relationship.

⁴⁵⁰ The stratiform cross-section at 0000 UTC (Fig. 7a) reveals layered echoes, with a broad re-
⁴⁵¹ gion of stratiform rain at low-levels and weaker echoes aloft associated with ice and snow. The
⁴⁵² wind vectors show increasing easterly flow with height and only weak vertical velocity, with lit-
⁴⁵³ tle indication of individual convective cores. Stratiform precipitation processes produce mid-level
⁴⁵⁴ convergence (not shown) with weak updrafts above the melting level and downdrafts below it. The
⁴⁵⁵ cross-section indicates a $8 \times 10^{-4} \text{ s}^{-1}$ vorticity maximum near 6 km, suggesting positive stretching
⁴⁵⁶ of the background vorticity associated with the mid-level convergence.

⁴⁵⁷ In contrast, the convective cross-section at 1200 UTC (Fig. 7b) reveals cellular echoes, with
⁴⁵⁸ strong reflectivity near 40 dBZ at low-levels and echo tops reaching 16 km altitude in the deepest
⁴⁵⁹ convection. Stronger updrafts are apparent in the predominately westerly flow, with some weak
⁴⁶⁰ easterlies associated with flanking subsidence to the east of the convective tower. Low-level con-
⁴⁶¹ vergence (not shown) associated with the active convection positively stretches local vorticity and
⁴⁶² results in the maximum vorticity at low-levels. Upper-level divergence in the convective outflow
⁴⁶³ compresses vortex tubes and results in a corresponding negative vorticity maximum aloft. Some of
⁴⁶⁴ the negative vorticity aloft is also likely associated with vorticity dipoles from tilting of horizontal
⁴⁶⁵ vorticity as seen in Fig. 5b.

⁴⁶⁶ The observed convective and vorticity patterns on both the meso- α and meso- β scale are con-
⁴⁶⁷ sistent with the known divergence profiles and implied vortex stretching for active deep convective
⁴⁶⁸ and older stratiform precipitation processes (Mapes and Houze 1995). The two precipitation types
⁴⁶⁹ directly contribute to the low-level and mid-level spin-up, respectively. A key question is why the
⁴⁷⁰ convective character changed over this 12-hour period. To address this question, the difference

471 in the thermodynamic properties of the meso- α scale analyses averaged over the 600 x 600 km
472 domain were examined.

473 Figure 8a shows the vertical profile of average differences of several thermodynamic variables
474 between the two aircraft missions. The differences were calculated by averaging over the meso- α
475 scale domain at 1200 and 0000 UTC and subtracting the mean values. Inflection points near 4 and
476 12 km altitude approximately separate the changes at low, mid, and upper-levels. The potential
477 temperature (θ , green dashed line) decreased slightly at low-levels and upper-levels and increased
478 slightly mid-levels in the overnight hours. Since the change in the average θ value represents
479 diabatic effects in clear air and clouds from both radiation and water phase changes, we can only
480 speculate as to the dominant processes. Upper-level cooling is consistent with radiation from
481 cloud-tops. The low-level cooling is consistent with both radiation from the surface and lower-
482 tropospheric water vapor, as well as evaporative cooling from the widespread stratiform rain. The
483 slight mid-level warming in θ may be due to longwave warming and latent heating in clouds or
484 balanced temperature responses associated with gradient wind adjustment. As will be shown later,
485 the low-level virtual potential temperature oscillates with a period close to diurnal time-scale,
486 while the mid-level temperature generally increases over time.

487 The water vapor mixing ratio (q_v , purple solid line) increased at low-levels, decreased slightly
488 at mid-levels, and showed minimal change at upper-levels. These changes are consistent with the
489 microphysical effects of stratiform precipitation. The low-level increase is consistent with rain
490 evaporation in the stratiform MCS, but detrainment from shallow and congestus convection and
491 dynamical impacts from moisture convergence may also have contributed. The decrease in mixing
492 ratio above the freezing level is consistent with vapor deposition of ice crystals, but moisture
493 divergence may also have played a role. Smaller amounts of water vapor at upper-levels showed
494 little change. The changes in θ and q_v affect the equivalent potential temperature (θ_e , black dotted

line) in generally opposite ways. The moisture changes at low to mid-levels have a larger effect on θ_e than temperature changes, such that the θ_e increased below 4 km altitude and decreased in the middle troposphere. At upper-levels, θ and θ_e were approximately the same due to limited water vapor capacity.

We argue that the extensive stratiform precipitation in the preceding 12 hours played both a dynamic and a thermodynamic role in aiding the early morning deep convective bursts around 1200 UTC. From a dynamical perspective, stratiform mid-level convergence increased the depth of the recirculating flow and the protective pouch that reduced environmental dry-air intrusions on the circulation. The strong correlation between RH and vorticity in the meso- α scale analyses supports this hypothesis. From a thermodynamic perspective, evaporative cooling and moistening of the lower troposphere from stratiform rain that was positively phased with diurnal cooling provided an additional benefit for subsequent convection. The dramatic increase in convective activity (Davis and Ahijevych 2012) is consistent with the observed power law increase in precipitation above a critical value of total column water vapor and saturation fraction (Neelin et al. 2009). Both the onset of deep convection (Holloway and Neelin 2009) and the strength of updrafts and downdrafts (James and Markowski 2010; Kilroy and Smith 2012) have been shown to have a strong relationship with lower tropospheric moisture due to the effects of entrainment on parcel buoyancy above the boundary layer.

The conceptual model presented here bears some similarity with that described by Mapes and Houze (1995) to explain an MCS observed in Tropical Cyclone Oliver (1993). In this model, the deep convective heating results as an opposing response to the thermal anomalies associated with stratiform heating. The stratiform MCS precipitation produces favorable thermodynamic conditions for subsequent deep convection and convective heating that work to eliminate the low-level cool anomaly. Favorable phasing with the diurnal cycle appears to have aided these conditions in

519 pre-depression Karl. A key addition to this conceptual model in the genesis context is the dynamical
520 environment of the pouch, allowing for repeated moistening of air parcels after each convective
521 cycle as the disturbance moves northwestward. As will be shown below, the thermal anomalies
522 oscillated with time in a similar manner to the circulation that is consistent with this conceptual
523 model.

524 **4. Circulation dynamics on the meso- α scale**

525 The analyses presented in the previous section focused on a 12-hour period on 13 September to
526 illustrate the proposed mechanisms for intensifying the pre-depression prior to genesis. To pro-
527 vide further evidence that vortex stretching resulting from the convective activity was the primary
528 mechanism for spin-up, a circulation budget in the meso- α scale domain was performed.

529 Figure 8b shows the vertical profile of average absolute vorticity over the meso- α scale domain
530 at the two times. The mean vorticity was maximized at mid-levels at 0000 UTC (blue solid line)
531 and decreased towards the surface. At 1200 UTC (red dashed line) the vorticity increased at low-
532 levels and decreased at mid- to upper-levels. The changes in the vertical absolute vorticity profile
533 are consistent with the meso- β analyses and the vertical divergence profiles of stratiform and deep
534 convective precipitation. The two precipitation regimes alternatively spin-up and down the mid
535 and low-level circulations, with deep convective bursts that transition to stratiform rain, that then
536 pre-condition the next convective burst.

537 The contributions to circulation tendency for these two analyses times are shown in Fig. 9. At
538 both times, the net tendency obtained from summation of the component terms was dominated
539 by the mean stretching term, with non-negligible contributions from eddy fluxes. Due to the
540 large meso- α scale domain, the average vertical velocity was minimal at the perimeter resulting
541 in no significant contribution from tilting. At 0000 UTC (Fig. 9a), the circulation tendency was

542 dominated by the vertical divergence profile associated with stratiform precipitation. Mean mid-
543 level convergence with low and upper-level divergence in the cyclonic flow resulted in spin-up
544 of the mid-level circulation with spin-down above and below. Eddy fluxes generally opposed the
545 stretching tendency, but with a smaller magnitude. Friction contributed to spin-down below 800
546 hPa, but was much smaller than the leading order terms. In contrast to previous interpretations
547 (Bister and Emanuel 1997), the circulation tendency suggests that the large stratiform mid-level
548 circulation was not building down toward the surface, and in fact was negatively impacting the
549 low-level circulation.

550 In addition to the direct spin-down of the circulation by friction at the perimeter, frictional forc-
551 ing induces convergence near the surface and divergence above the boundary layer through an
552 Ekman layer flow. The calculated stretching tendency below 800 hPa is likely a combination of
553 both the stratiform divergence and secondary frictional effects. Frictional convergence offsets the
554 stratiform divergence near the surface, but the net effect is a spin-down of the vortex above the
555 boundary layer. The circulation tendency suggests that the vortex would lose approximately 35%
556 of the equivalent circulation of the Coriolis parameter at this latitude in the 12 hours between mis-
557 sions at 850 hPa due to the low-level divergence. However, the circulation tendency was clearly
558 not constant over this period so that is a very rough estimate.

559 At 1200 UTC (Fig. 9b), the circulation tendency was dominated by the vertical divergence
560 profile associated with convective precipitation. Strong low-level convergence and weak eddy
561 fluxes result in spin-up below 700 hPa that is maximized near the surface. Positive tendencies
562 below 700 hPa approximately equal or exceed the spin-down seen 12 hours before, consistent
563 with a net low-level spin-up over this time period. Mid- and upper-level divergence result in spin-
564 down above 700 hPa that is offset by positive eddy fluxes above 300 hPa. There are no obvious
565 secondary frictional effects in the profile at this time, but presumably the decreasing convergence

566 with height may be partially a result of these effects. The weaker eddy fluxes may be a result of
567 decreasing vertical shear between 925 and 500 hPa at this time (Davis and Ahijevych 2012).

568 Lussier et al. (2014) demonstrated that the specific area chosen to calculate the circulation
569 budget can affect the interpretation. In order to verify that our interpretation is not overly sensitive
570 to the choice of the budget domain, the magnitude of the mean absolute vorticity (e.g. circulation)
571 and mean stretching tendency calculated using different sized boxes is shown in Fig. 10. The sign
572 of the stretching term is largely insensitive to the domain size, except for the region below 950 hPa
573 at 0000 UTC (Fig. 10). The tendency due to mean stretching is slightly above zero if the domain
574 box length is smaller than 250 km from the center (e.g. 500 x 500 km across), but is negative
575 using a larger box. However, the general pattern of stronger positive stretching at mid-levels, and
576 negative or near zero stretching at mid-levels does not depend on the domain size.

577 The structure of the mean absolute vorticity at 0000 UTC is also relatively insensitive to the
578 domain size, but the magnitude does increase as the box gets smaller. The maximum vorticity
579 at mid-levels is consistent with the stretching tendency pattern and the presence of widespread
580 stratiform convection. At 1200 UTC, the sign of the stretching term is the same with changing box
581 size except for the region near 400 hPa outside of 300 km. The maximum in positive stretching is
582 slightly higher inside of 150 km, but a deep layer of positive stretching up to 650 hPa is apparent
583 at all domain sizes. The mean vorticity maximum has a lower magnitude than at 0000 UTC, but
584 it likewise increases as the box gets smaller. Fig. 10 confirms that the circulation tendencies and
585 vorticity structure are not overly sensitive to the domain size, and that the 300 km radius seems to
586 be a reasonable choice for assessing the bulk meso- α scale circulation evolution and tendencies.
587 Using a smaller radius only magnifies the amplitude of the vorticity and tendencies, consistent
588 with the evolution depicted in Fig. 2.

589 The circulation tendencies provide additional evidence that the meso- α circulation was strongly
590 affected by the convective activity, and that a transition from predominately stratiform to deep
591 convective activity occurred over the 12-hour period. The analyses support the hypothesis that
592 active deep convection was the primary low-level spin-up mechanism and stratiform precipitation
593 was the primary mid-level spin-up mechanism, but these illustrations are only snapshots of the pre-
594 depression period. Observational evidence from PREDICT suggests that more than one convective
595 burst is typically required for genesis to occur (Montgomery et al. 2012). Karl's pre-depression
596 period was characterized by a series of early morning deep convective bursts followed by stratiform
597 transitions, which are believed to have collectively led to genesis after several days.

598 A time series of the meso- α scale characteristics leading up to genesis is shown in Fig. 11. The
599 symbols are plotted at the analysis times when research observations were available, denoted by
600 the red stars at the bottom of the figure. The two research missions on 13 September described in
601 detail above are highlighted. In Fig. 9a, the circulation tendencies from mean stretching at 850
602 (red circles) and 500 hPa (blue squares) show an alternating oscillation through the pre-depression
603 period. Periods of low-level spin-up correspond to periods of mid-level spin-down, and mid-level
604 spin-up corresponds to low-level spin-down. Note that the lines connecting each mission are just
605 linear interpolations, and do not capture higher frequency changes on the meso- α scale.

606 The time series of CCF illustrates the relationship between the circulation tendencies and con-
607 vective activity. The low-level spin-up tendencies correspond to the peaks in CCF, strongly sug-
608 gesting that the low-level stretching was associated with the repeated deep convective bursts. Mid-
609 level spin-up tendencies correspond to the time periods shortly after the peak CCF as cloud-tops
610 warmed, suggesting that the mid-level stretching was associated with the stratiform transitions.

611 Saturation fraction (SF) from 1000 to 700 hPa (green triangles) shows the integrated RH in the
612 lower troposphere. The SF time series indicates a positive, in-phase relationship between available

water vapor, the convective bursts, and the low-level spin-up tendencies. Active convective periods were characterized by SF above 0.85, suggesting a possible critical value for the onset of deep convection. The 0.85 value is similar to the critical values reported by Neelin et al. (2009) for tropical convection.

A time series of thermodynamic variables is shown in Fig. 11b. The RH at 850 hPa (green triangle) oscillated around 85%, similar to the SF integrated through 700 hPa shown in Fig. 11a. The strong relationship between RH at this level and SF is consistent with the results of Holloway and Neelin (2009) that show a maximum in the water vapor variance in the tropics at 850 hPa. The virtual potential temperature (θ_v , purple squares) at 850 hPa oscillated with the diurnal and convective cycle, but also increased over the pre-depression period. A diurnal timescale explains 85% of the variance in 850 hPa θ_v time series, consistent with the conceptual model of diurnal and convective heating and cooling presented earlier.

A weaker θ_v oscillation is seen at 500 hPa (black diamonds) that was out of phase with the low-level temperature oscillation before 13 September, but then increased steadily. The 500 hPa temperature increase is consistent with a balanced temperature response to increasing positive vorticity anomalies at and below this level seen in dropsonde composites of developing disturbances (Davis and Ahijevych 2013; Komaromi 2012; Raymond 2012). The dropsonde composites had cold low-level virtual temperature anomalies compared with various environmental reference states. An important distinction between the SAMURAI analysis of Karl and the composite profiles of those studies is the lack of low-level cooling over the pre-depression period. The current analyses are more consistent with the results of Smith and Montgomery (2012) that showed warming at all levels over time in their composites. Although the low-level θ_v may indeed be cold compared to non-developing disturbances, the temperature trends do not suggest that progressive

636 low-level cooling was important in Karl's genesis process, but rather suggest the importance of
637 episodic low-level cooling that produced favorable conditions for the onset of deep convection.
638 Comparison of Figs. 11a and b reveal that increases in 850 hPa circulation are in phase with
639 increases in RH and 500 hPa θ_v , and decreases in 850 hPa θ_v . The phasing of the dynamic and
640 thermodynamic variables in the time series is consistent throughout the pre-depression period.
641 Correlation coefficients between the 850 hPa stretching tendency and RH time series were above
642 0.6 at all pressure levels below 700 hPa, with a maximum value of 0.78 at the 850 hPa level.
643 Negative correlation with θ_v below 700 hPa with similar magnitudes suggest a prominent role of
644 the diurnal and convective cycle in the meso- α scale RH time series. Positive correlations ranging
645 between 0.2 and 0.6 of the stretching tendency with q_v time series below 700 hPa (not shown)
646 suggest that moisture recovery was also important to the convective processes.

647 5. Discussion and Conclusions

648 Observations of the mesoscale processes leading to tropical cyclogenesis were collected as part
649 of the PREDICT, GRIP, and IFEX field campaigns during the summer of 2010. Eight research
650 aircraft missions over the five days prior to the genesis of Hurricane Karl provided Doppler radar,
651 in situ flight level, and dropsonde data documenting the structural changes of the pre-depression
652 disturbance. The research observations were combined here with satellite atmospheric motion
653 vectors and *a priori* background estimates of the atmospheric state from the ECMWF 25-km global
654 analyses using a spline-based variational technique called SAMURAI. While the observations
655 were not continuous in time, the SAMURAI analyses at the meso- β and meso- α scales following
656 the pre-Karl wave pouch provide a consistent and unprecedented depiction of the evolution of the
657 thermodynamics and dynamics in the pre-depression period.

658 Low-level spin-up of the meso- α scale cyclonic circulation occurred during periods of active
659 deep convection, with circulation analysis indicating that the positive tendencies were largely due
660 to vortex tube stretching from mean convergence of perimeter-averaged vorticity. Active con-
661 vective periods were also characterized by spin-down of the mid-level circulation associated with
662 mean divergence. As the convective bursts waned and transitioned to predominately stratiform
663 mesoscale convective systems, the circulation tendencies transitioned to a complementary signa-
664 ture of low-level spin-down and mid-level spin-up corresponding with the divergence profile of
665 stratiform precipitation. The changes in meso- α scale circulation due to tendencies from vortex
666 stretching were consistent with the contributions from each predominant precipitation mode. The
667 circulation tendencies for closed circuits that encompass the pouch suggest that the conclusions are
668 not overly sensitive to the choice of the domain size, but the magnitudes of stretching tendencies
669 and circulation increase as the domain size decreases to the meso- β scale around the sweet spot
670 region of the pouch, consistent with Wang (2012). Doppler radar analyses on the meso- β scale on
671 13 September confirmed the kinematic and precipitation structure deduced from dropsondes and
672 satellite imagery, and showed the presence of low-level and mid-level vorticity maxima co-located
673 with convective and stratiform precipitation features, respectively.

674 The low-level and mid-level vorticity and moisture fields appear to be strongly linked throughout
675 the pre-genesis period. Specifically, a series of convective bursts occurred near the sweet spot
676 within the high vorticity recirculation region, predominately in the early morning. The meso-
677 α scale thermodynamic environment during the bursts was characterized by enhanced relative
678 humidity in a deep layer, with saturation fraction typically near 0.85 for a layer between the surface
679 and 700 hPa. These results are consistent with the concept of a critical threshold for the onset of
680 deep convection in the tropics (Neelin et al. 2009). High relative humidity throughout the lower

681 troposphere would support deep convection by reducing dry air entrainment, thereby maintaining
682 entraining parcel buoyancy through a deeper layer.

683 The enhanced relative humidity was due to both reduced potential temperature and enhanced
684 specific humidity. These characteristics are thought to be the result of both diurnal radiational
685 cooling and evaporative cooling in stratiform rain in the overnight hours. The cycle of deep con-
686 vection and stratiform transitions was in phase with the diurnal cycle, suggesting the time scale
687 for boundary layer moisture and CAPE recovery was similar to the diurnal period consistent with
688 Li et al. (2006). We speculate that disturbances with forced convective episodes due to stronger
689 vertical shear that are not in phase with the diurnal cycle would be less favorable for development.
690 Further research on the relevant thermodynamic time scales in pre-depressions and their phasing
691 is recommended.

692 Composite dropsonde studies from PREDICT have suggested that higher available moisture
693 above the boundary layer was a critical distinguishing factor between developing and non-
694 developing disturbances (Smith and Montgomery 2012; Komaromi 2012; Davis and Ahijevych
695 2013). In some respects, the thermodynamic impact of cooling and moistening by stratiform rain
696 prior to deep convection is similar to that proposed by Bister and Emanuel (1997), but we empha-
697 size here the role of moistening in reducing entrainment in subsequent deep convection (James
698 and Markowski 2010; Kilroy and Smith 2012). Bister and Emanuel (1997, p. 2667) further argue
699 that “the stratiform rain must last long enough to drive the midlevel vortex down to the boundary
700 layer”. Our results do not support this hypothesis, and instead suggest that subsequent deep con-
701 vection is required to spin-up the low-level circulation. The low-level spin-down associated with
702 the stratiform periods suggest that a negative dynamic impact of the stratiform divergence profile
703 was to weaken the near-surface circulation. We hypothesize that the positive dynamic impact of
704 the stratiform MCSs was to enhance the mid-level pouch through vortex stretching, allowing for

705 protection from the environmental dry air and continued moistening of air parcels through a deeper
706 layer. This indirect effect provided a favorable thermodynamic environment for the repeated onset
707 of deep convection within the parent synoptic-scale wave as it moved northwestward.

708 The results from this study suggest the convective cycle in Karl alternately built the low and
709 mid-level circulations leading to genesis as summarized in the following sequence of events. The
710 initial environment for the development of deep convection was a modest low-level circulation
711 on the meso- α scale with no substantial mid-level circulation on 10 September. A strong con-
712 vective burst then erupted in the vorticity rich environment on the morning of 11 September that
713 enhanced the low-level circulation. As the convection waned, the resulting transition to stratiform
714 MCSs strengthened the mid-level pouch through mid-level convergence and vortex stretching as-
715 sociated with ice microphysical processes, and protected the disturbance from the intrusion of dry
716 environmental air. Low-level divergence associated with the stratiform rain acts to spin down the
717 low-level circulation, but surface moisture fluxes and cooling associated with rain evaporation and
718 the diurnal minimum helps to increase the relative humidity, lower the level of free convection,
719 and condition the environment for another burst of deep convection. Once the column satura-
720 tion reaches a critical value, a subsequent convective burst below the mid-level circulation further
721 enhances the low-level circulation, and the convective cycle repeats.

722 While cooling from evaporation and radiation appears to have provided an important modulation
723 of temperature, the analysis indicates a warming trend at nearly all levels leading to genesis. The
724 warming was greatest at mid-levels, but was non-negligible at low-levels above the boundary layer.
725 We note that the negative temperature anomalies observed by Davis and Ahijevych (2013) and
726 Komaromi (2012) were relative to an environmental reference state, but did not appear to get
727 significantly stronger over time during the pre-depression period when averaged over all cloud
728 types on a domain with a similar size to that used here. The warming trend in the current analysis

729 is consistent with the analysis of Smith and Montgomery (2012), suggesting that the interpretation
730 of the low-level cold anomaly appears to depend strongly on the analysis technique, domain size,
731 and temporal scale. Our analysis suggests that a balanced increasing warm core in the mid- to
732 upper-troposphere was the result of the increasing circulation during the pre-depression period,
733 and no transition from a cold-core structure was required.

734 The results suggest further that there was no sustained lowering of the mass flux due to the
735 increased stabilization as hypothesized by Komaromi (2012), Raymond (2012), Gjorgjievska and
736 Raymond (2014), and Davis and Ahijevych (2013). While the analyses are not inconsistent with
737 increasing stabilization as described by the foregoing studies, the results show episodic low-level
738 convergence due to repeated convective bursts within pre-Karl's recirculating pouch region. Our
739 interpretation of the observational analysis presented in this study provides a novel hypothesis for
740 the supporting role of stratiform precipitation in the maintenance of the mid-level cyclonic pouch
741 as a moisture containment vessel within the context of the marsupial paradigm. Our interpretation
742 reaffirms also a primary role of deep convection in the genesis process. The analyses suggest that
743 the onset of deep convection and associated low-level spin-up was closely related to the coupling of
744 the vorticity and moisture fields at low and mid-levels. Further detailed case studies of developing
745 and non-developing storms are necessary to further assess the hypothesis presented herein.

746 *Acknowledgments.* This study was supported by the National Science Foundation (NSF)
747 award AGS-0851077. MMB also acknowledges support by the NSF CAREER award AGS-
748 1701225 and the Office of Naval Research (ONR) Director of Research Early Career Grant
749 N000141613033. MTM acknowledges the support of NSF grant AGS-1313948, NOAA HFIP
750 grant N0017315WR00048, NASA grant NNG11PK021, ONR grant 0001417WX00336, and the
751 U. S. Naval Postgraduate School. The authors would like to thank the PREDICT, GRIP, and IFEX

752 teams for collecting the data used in this study. We would also like to thank David Raymond and
753 two anonymous reviewers for their insightful reviews that improved the manuscript. All code and
754 data used in this study is available upon request.

755 **References**

- 756 Bell, M. M., and M. T. Montgomery, 2010: Sheared deep vertical convection in pre-depression
757 Hagupit during TCS-08. *Geophys. Res. Lett.*, **37**, L06 802, doi:10.1029/2009GL042 313.
- 758 Bell, M. M., M. T. Montgomery, and K. A. Emanuel, 2012: Air-sea enthalpy and momentum
759 exchange at major hurricane wind speeds. *J. Atmos. Sci.*, **69**, 3197–3122.
- 760 Bister, M., and K. A. Emanuel, 1997: The genesis of Hurricane Guillermo: TEXMEX analyses
761 and a modeling study. *Mon. Wea. Rev.*, **125**, 2662–2682.
- 762 Bosart, B. L., W.-C. Lee, and R. M. Wakimoto, 2002: Procedures to improve the accuracy of
763 airborne Doppler radar data. *J. Atmos. Oceanic Technol.*, **19**, 322–339.
- 764 Davis, C., and D. Ahijevych, 2012: Mesoscale structural evolution of three tropical weather sys-
765 tems observed during PREDICT. *J. Atmos. Sci.*, **69**, 1284–1305.
- 766 Davis, C., and D. Ahijevych, 2013: Thermodynamic environments of deep convection in Atlantic
767 tropical disturbances. *J. Atmos. Sci.*, **70**, 1912–1928.
- 768 Davis, C., and T. Galarneau, 2009: The vertical structure of mesoscale convective vortices. *J.*
769 *Atmos. Sci.*, **66**, 686–704.
- 770 Dunkerton, T. J., M. T. Montgomery, and Z. Wang, 2009: Tropical cyclogenesis in a tropi-
771 cal wave critical layer: easterly waves. *Atmos. Chem. and Phys.*, **9**, 5587–5646, doi:10.5194/
772 acp-9-5587-2009.

- 773 Foerster, A. M., and M. M. Bell, 2017: Thermodynamic retrieval in rapidly rotating vortices from
774 multiple-Doppler radar data. *J. Atmos. Oceanic Technol.*, **34**, 2353–2374.
- 775 Foerster, A. M., M. M. Bell, P. A. Harr, and S. C. Jones, 2014: Observations of the eyewall
776 structure of Typhoon Sinlaku (2008) during the transformation stage of extratropical transition.
777 *Mon. Wea. Rev.*, **142**, 3372–3392.
- 778 Frank, N. L., 1970: Atlantic tropical systems of 1969. *Mon. Wea. Rev.*, **98**, 307–314.
- 779 Freismuth, T. M., B. Rutherford, M. A. Boothe, and M. T. Montgomery, 2016: Why did the storm
780 ex-Gaston (2010) fail to redevelop during the PREDICT experiment? *Atmos. Chem. and Phys.*,
781 **16**, 8511–8519, doi:10.5194/acp-16-8511-2016.
- 782 Gjorgjievska, S., and D. J. Raymond, 2014: Interaction between dynamics and thermody-
783 namics during tropical cyclogenesis. *Atmos. Chem. and Phys.*, **14**, 3065–3082, doi:10.5194/
784 acp-14-3065-2014.
- 785 Gray, W. M., 1968: Global view of the origin of tropical disturbances and storms. *Mon. Wea. Rev.*,
786 **96**, 669–700.
- 787 Haynes, P. H., and M. E. McIntyre, 1987: On the evolution of vorticity and potential vorticity
788 in the presence of diabatic heating and frictional or other forces. *J. Atmos. Sci.*, **44**, 828–841,
789 doi:10.1175/1520-0469(1987)044<0828:OTEVOVA>2.0.CO;2.
- 790 Hendricks, E. A., M. T. Montgomery, and C. A. Davis, 2004: The role of “vortical” hot towers in
791 the formation of Tropical Cyclone Diana (1984). *J. Atmos. Sci.*, **61**, 1209–1232.
- 792 Holloway, C. E., and J. D. Neelin, 2009: Moisture vertical structure, column water vapor, and
793 tropical deep convection. *J. Atmos. Sci.*, **66**, 1665–1683.

- 794 Houze, R. A., W.-C. Lee, and M. M. Bell, 2009: Convective contribution to the genesis of Hurri-
- 795 cane Ophelia (2005). *Mon. Wea. Rev.*, **137**, 2778–2800.
- 796 James, R. P., and P. M. Markowski, 2010: A numerical investigation of the effects of dry air aloft
- 797 on deep convection. *Mon. Wea. Rev.*, **138**, 140–161.
- 798 Kilroy, G., and R. K. Smith, 2012: A numerical study of rotating convection during tropical
- 799 cyclogenesis. *Quart. J. Roy. Meteor. Soc.*, **139**, 1255–1269, doi:10.1002/qj.2022.
- 800 Komaromi, W., 2012: An investigation of composite dropsonde profiles for developing and nonde-
- 801 veloping tropical waves during the 2010 PREDICT field campaign. *J. Atmos. Sci.*, **70**, 542–558.
- 802 Li, T., X. Ge, B. Wang, and Y. Zhu, 2006: Tropical cyclogenesis associated with rossby wave
- 803 energy dispersion of a preexisting typhoon. part ii: Numerical simulations. *J. Atmos. Sci.*, **63**,
- 804 1390–1409.
- 805 Lussier, L. L., M. T. Montgomery, and M. M. Bell, 2014: The genesis of Typhoon Nuri as observed
- 806 during the Tropical Cyclone Structure 2008 (TCS08) field experiment - Part 3: Kinematical and
- 807 dynamical aspects of genesis. *Atmos. Chem. and Phys.*, **14**, 8795–8812.
- 808 Mapes, B. E., and R. A. Houze, Jr., 1995: Diabatic divergence profiles in western pacific mesoscale
- 809 convective systems. *J. Atmos. Sci.*, **52**, 1807–1828.
- 810 Marks, F. D., and R. A. Houze, 1987: Airborne doppler radar observations in hurricane debby.
- 811 *Bull. Amer. Meteor. Soc.*, **65**, 569–582.
- 812 McBride, J. L., and R. Zehr, 1981: Observational analysis of tropical cyclone formation. part ii:
- 813 Comparison of non-developing versus developing systems. *J. Atmos. Sci.*, **38**, 1132–1151.
- 814 Melhauser, C., and F. Zhang, 2014: Diurnal radiation cycle impact on the pregenesis environment
- 815 of Hurricane Karl (2010). *J. Atmos. Sci.*, **71**, 1241–1259.

- 816 Montgomery, M. T., M. M. Bell, S. D. Aberson, and M. L. Black, 2006: Hurricane Isabel (2003):
817 New insights into the physics of intense storms. Part I: Mean vortex structure and maximum
818 intensity estimates. *Bull. Amer. Meteor. Soc.*, **87**, 1335–1347.
- 819 Montgomery, M. T., R. Smith, and S. Nguyen, 2010: Sensitivity of tropical cyclone models to the
820 surface drag coefficient. *Quart. J. Roy. Meteor. Soc.*, **136**, 1945–1953.
- 821 Montgomery, M. T., and R. K. Smith, 2012: The genesis of Typhoon Nuri as observed during the
822 Tropical Cyclone Structure 2008 (TCS08) field experiment – Part 2: Observations of the con-
823 vective environment. *Atmos. Chem. and Phys.*, **12**, 4001–4009, doi:10.5194/acp-12-4001-2012.
- 824 Montgomery, M. T., and Coauthors, 2012: The Pre-Depression Investigation of Cloud Systems in
825 the Tropics (PREDICT) experiment: Scientific basis, new analysis tools and some first results.
826 *Bull. Amer. Meteor. Soc.*, **93**, 153–172.
- 827 Neelin, J. D., O. Peters, and K. Hales, 2009: The transition to strong convection. *J. Atmos. Sci.*,
828 **66**, 2367–2384.
- 829 Nguyen, V. S., R. K. Smith, and M. T. Montgomery, 2008: Tropical cyclone intensification and
830 predictability in three dimensions. *Quart. J. Roy. Meteor. Soc.*, **134**, 563–582.
- 831 Nolan, D. S., E. D. Rappin, and K. A. Emanuel, 2007: Tropical cyclogenesis sensitivity to environ-
832 mental parameters in radiative–convective equilibrium. *Quart. J. Roy. Meteor. Soc.*, **133 (629)**,
833 2085–2107, doi:10.1002/qj.170.
- 834 Raymond, D. J., 2012: Balanced thermal structure of an intensifying tropical cyclone. *Tellus A*,
835 **64**, 19 181.

- 836 Raymond, D. J., and M. M. Flores, 2017: Predicting convective rainfall over tropical oceans
837 from environmental conditions. *J. Adv. Model. Earth Syst.*, **8** (2), 703–718, doi:10.1002/
838 2015MS000595.
- 839 Raymond, D. J., and C. Lopez-Carillo, 2011: The vorticity budget of developing typhoon Nuri
840 (2008). *Atmos. Chem. and Phys.*, **11**, 142–163.
- 841 Raymond, D. J., C. Lopez-Carillo, and L. L. Cavazos, 1998: Case-studies of developing east
842 Pacific easterly waves. *Quart. J. Roy. Meteor. Soc.*, **124**, 2005–2034.
- 843 Raymond, D. J., and S. L. Sessions, 2007: Evolution of convection during tropical cyclogenesis.
844 *Geophys. Res. Lett.*, **34**, doi:10.1029/2006GL028607.
- 845 Raymond, D. J., S. L. Sessions, and C. L. Carrillo, 2011: Thermodynamics of tropical cyclogenesis
846 in the northwest pacific. *J. Geophys. Res. Atmos.*, **116** (D18), doi:10.1029/2011JD015624.
- 847 Reasor, P. D., M. T. Montgomery, and L. F. Bosart, 2005: Mesoscale observations of the genesis
848 of Hurricane Dolly (1996). *J. Atmos. Sci.*, **62**, 3151–3171.
- 849 Sanger, N. T., M. T. Montgomery, R. K. Smith, and M. M. Bell, 2013: An observational study of
850 tropical cyclone spinup in Supertyphoon Jangmi (2008) from 24 to 27 September. *Mon. Wea.
851 Rev.*, **142**, 3–28.
- 852 Simpson, J., E. Ritchie, G. J. Holland, J. Halverson, and S. Stewart, 1997: Mesoscale interactions
853 in tropical cyclone genesis. *Mon. Wea. Rev.*, **125**, 2643–2661.
- 854 Sippel, J. A., J. W. Nielsen-Gammon, and S. E. Allen, 2006: The multiple-vortex nature of tropical
855 cyclogenesis. *Mon. Wea. Rev.*, **134**, 1796–1814.
- 856 Smith, R. K., and M. T. Montgomery, 2012: Observations of the convective environment in devel-
857 oping and non-developing tropical disturbances. *Quart. J. Roy. Meteor. Soc.*, **137**, 1–18.

- 858 Wang, Z., 2012: Thermodynamic aspects of tropical cyclone formation. *J. Atmos. Sci.*, **69**, 2433 –
859 2451.
- 860 Wang, Z., M. T. Montgomery, and T. J. Dunkerton, 2010a: Genesis of Pre–Hurricane Felix (2007).
861 Part I: The role of the easterly wave critical layer. *J. Atmos. Sci.*, **67**, 1711–1729.
- 862 Wang, Z., M. T. Montgomery, and T. J. Dunkerton, 2010b: Genesis of Pre–Hurricane Felix (2007).
863 Part II: Warm core formation, precipitation evolution, and predictability. *J. Atmos. Sci.*, **67**,
864 1730–1744.
- 865 Wang, Z., M. T. Montgomery, and C. Fritz, 2012: A first look at the structure of the wave pouch
866 during the 2009 PREDICT–GRIP dry runs over the Atlantic. *Mon. Wea. Rev.*, **140**, 1144–1163.
- 867 Wissmeier, U., and R. K. Smith, 2011: Tropical cyclone convection: the effects of ambient vertical
868 vorticity. *Quart. J. Roy. Meteor. Soc.*, **137**, 845–857.
- 869 Zawislak, J., and E. J. Zipser, 2014: Analysis of the thermodynamic properties of developing and
870 nondeveloping tropical disturbances using a comprehensive dropsonde dataset. *Mon. Wea. Rev.*,
871 **142**, 1250–1264.
- 872 Zehr, R. M., 1992: Tropical Cyclogenesis in the Western North Pacific. Ph.D. thesis, Colorado
873 State University.
- 874 Zhang, J. A., R. F. Rogers, D. S. Nolan, and F. D. Marks, 2011: On the characteristic height scales
875 of the hurricane boundary layer. *Mon. Wea. Rev.*, **139**, 2523–2535.
- 876 Zipser, E. J., and C. Gautier, 1978: Mesoscale events within a GATE tropical depression. *Mon.*
877 *Wea. Rev.*, **106**, 789–805.

878 LIST OF TABLES

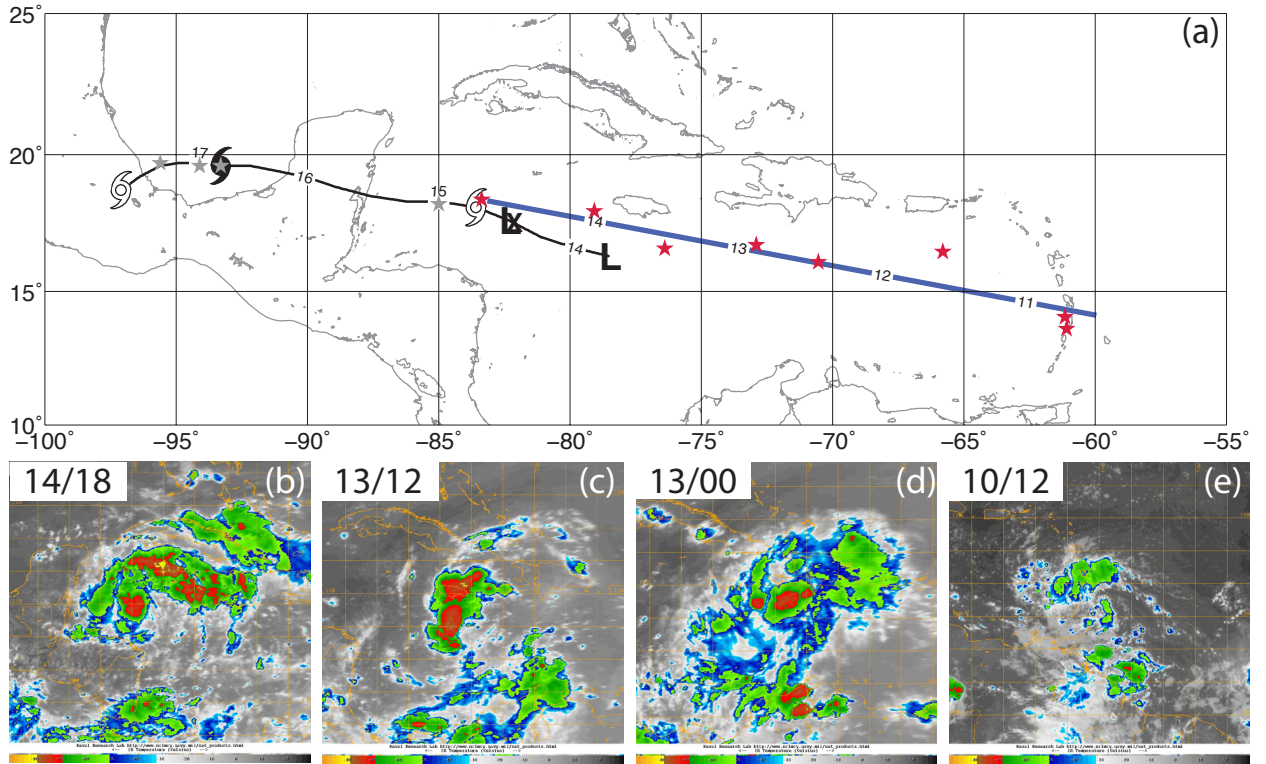
882 TABLE 1. Summary of SAMURAI settings and observations for meso- α and meso- β scale analyses.

883 Acronyms are Atmospheric Motion Vectors (AMV), and Tail Doppler Radar (TDR).

Setting	meso- α	meso- β
Horizontal node spacing	25 km	2 km
Horizontal error covariance length	100 km	8 km
Background u and v error σ	5 m s^{-1}	25 m s^{-1}
Background w error σ	1 m s^{-1}	25 m s^{-1}
Background T error σ	3 K	N/A
Background q_v error σ	1 g kg^{-1}	N/A
Observations analyzed	In situ, Dropsondes, AMVs	In situ, Dropsondes, AMVs, TDR

884 LIST OF FIGURES

- 885 **Fig. 1.** Track and infrared satellite snapshots of Hurricane Karl. Panel (a) shows linear pre-
886 depression track (thick blue line) derived from 850 hPa pouch centers at mission times
887 indicated by red stars, along with National Hurricane Center best track (thin black line)
888 and storm evolution (L denotes low, Lx denotes depression, open hurricane symbol denotes
889 tropical storm, and closed symbol denotes hurricane). Panels (b-e) show infrared satellite
890 imagery at key times. Satellite imagery courtesy Naval Research Laboratory Monterey. 42
- 891 **Fig. 2.** Analyzed time-series of meso- α absolute circulation from the initial aircraft mission to
892 Karl's genesis. Mean absolute circulation at 850 hPa (red circles) and 500 hPa (blue diamonds)
893 over the (a) 600 x 600 km domain and (b) 200 x 200 km domain centered on the
894 pouch correspond to the left abscissa. The fractional area of cloud tops below -60 °C taken
895 from Davis and Ahijeyvich (2012) corresponds to the right abscissa. Red stars at bottom of
896 figure denote mission times, with 0000 and 1200 UTC 13 September highlighted. 43
- 897 **Fig. 3.** Low-level meso- α and β structure at 0000 UTC 13 September. Panel (a) shows analyzed
898 meso- α absolute vertical vorticity (color, $3 \times 10^{-5} \text{ s}^{-1}$ interval), relative humidity (white,
899 10% contour interval), and wave-relative wind vectors (black) at 850 hPa. Red vectors
900 indicate measured dropsonde winds, and yellow box indicates area shown in panel (b). Red
901 star indicates location of the pouch 'sweet spot' as defined in the text. Panel (b) shows
902 analyzed meso- β radar reflectivity (color, 3 dBZ interval), absolute vertical vorticity ($20 \times$
903 10^{-5} s^{-1} contour interval, negative denoted by dashed lines), and wave-relative wind vectors
904 at 1.5 km altitude. 44
- 905 **Fig. 4.** Mid-level meso- α and β structure at 0000 UTC 13 September. Panels are the same as Fig.
906 3 except at (a) 500 hPa and (b) 6 km altitude. Absolute vertical vorticity contours in (b) are
907 lightened for clarity. 45
- 908 **Fig. 5.** Low-level meso- α and β structure at 1200 UTC 13 September. Panels are the same as Fig. 3. 46
- 909 **Fig. 6.** Mid-level meso- α and β structure at 1200 UTC 13 September. As in Figure 4, contours in
910 panel (b) are lightened for clarity. 47
- 911 **Fig. 7.** Radar vertical cross-sections showing radar reflectivity (color), absolute vertical vorticity
912 ($40 \times 10^{-5} \text{ s}^{-1}$ contour interval, negative denoted by dashed lines), and wave-relative wind
913 vectors at (a) 0000 UTC and (b) 1200 UTC 13 September. Cross-sections are taken along
914 (a) Y=26 km and (b) Y = -24 km in Figs. 3 and 5, respectively. 48
- 915 **Fig. 8.** Thermodynamic and vorticity differences on 600 x 600 km with height of meso- α averaged
916 quantities from 0000 to 1200 UTC 13 September. Panel (a) shows difference (1200 UTC
917 - 0000 UTC) of vapor mixing ratio (solid purple in g kg^{-1}), potential temperature (dashed
918 green in K), and equivalent potential temperature (dotted black in K). Panel (b) shows meso-
919 α scale averaged vorticity at 0000 UTC (solid blue) to 1200 UTC (dashed red) with height.
920 49
- 921 **Fig. 9.** Meso- α scale (600 x 600 km) circulation tendencies with height at (a) 0000 UTC and (b)
922 1200 UTC 13 September. Budget terms are mean stretching tendency (solid blue), eddy
923 flux tendency (dash-dot red), tilting tendency (long dash gray), friction tendency (short dash
924 purple), and net tendency calculated by summation of the component tendencies (thick solid
925 black line). 50



936 FIG. 1. Track and infrared satellite snapshots of Hurricane Karl. Panel (a) shows linear pre-depression track
 937 (thick blue line) derived from 850 hPa pouch centers at mission times indicated by red stars, along with National
 938 Hurricane Center best track (thin black line) and storm evolution (L denotes low, Lx denotes depression, open
 939 hurricane symbol denotes tropical storm, and closed symbol denotes hurricane). Panels (b-e) show infrared
 940 satellite imagery at key times. Satellite imagery courtesy Naval Research Laboratory Monterey.

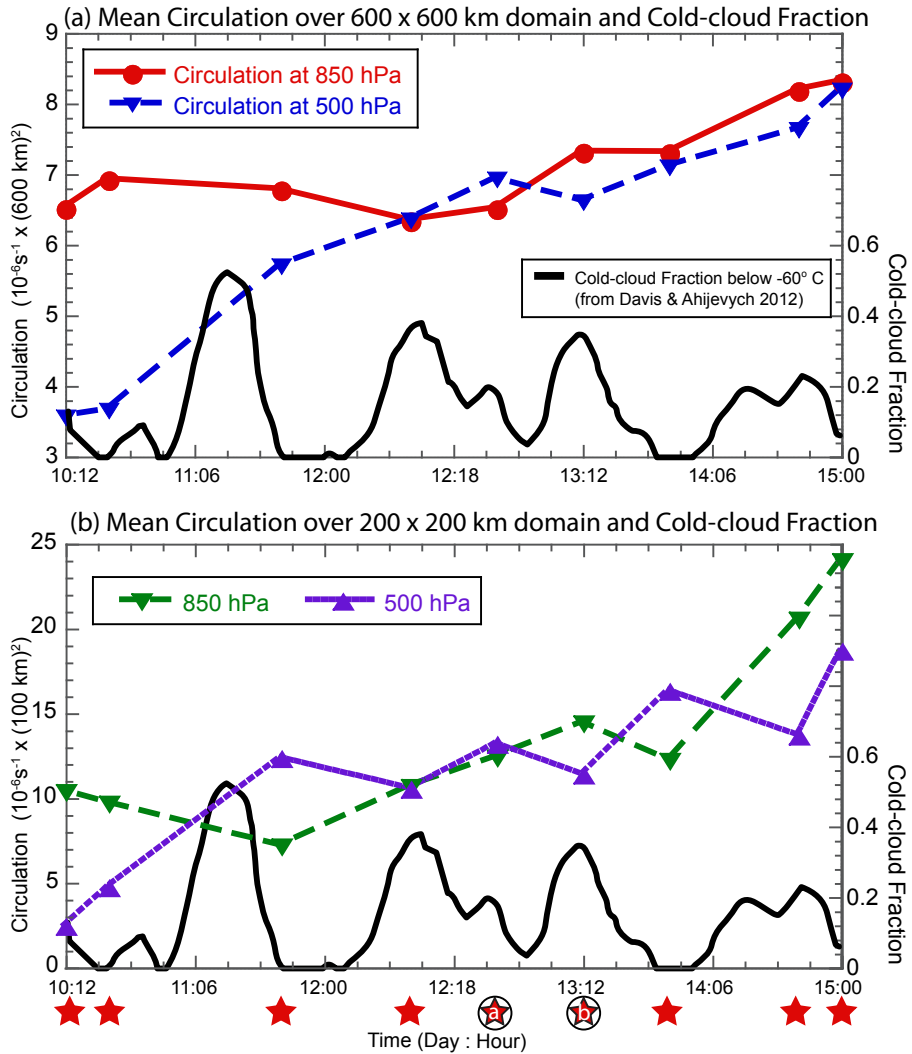


FIG. 2. Analyzed time-series of meso- α absolute circulation from the initial aircraft mission to Karl's genesis.
 Mean absolute circulation at 850 hPa (red circles) and 500 hPa (blue diamonds) over the (a) 600 x 600 km domain and (b) 200 x 200 km domain centered on the pouch correspond to the left abscissa. The fractional area of cloud tops below -60°C taken from Davis and Ahijevych (2012) corresponds to the right abscissa. Red stars at bottom of figure denote mission times, with 0000 and 1200 UTC 13 September highlighted.

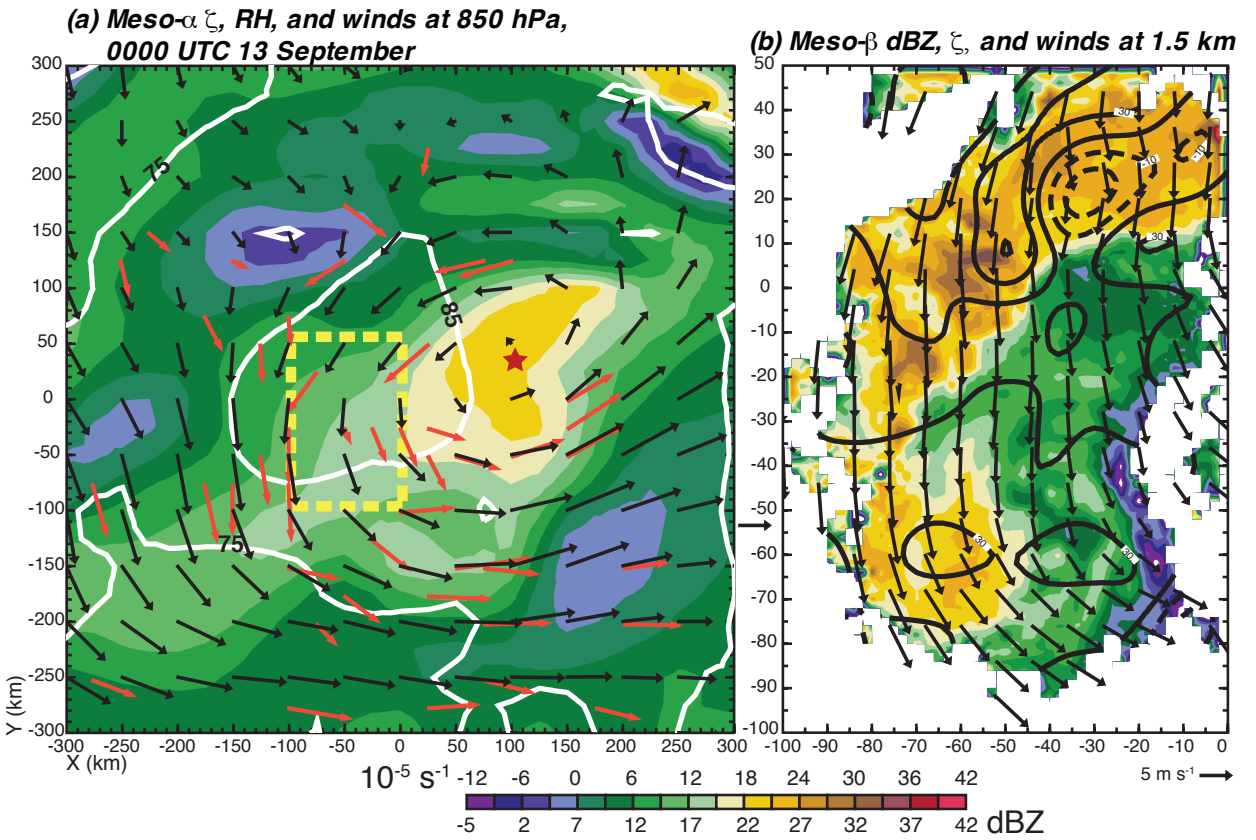


FIG. 3. Low-level meso- α and β structure at 0000 UTC 13 September. Panel (a) shows analyzed meso- α absolute vertical vorticity (color, $3 \times 10^{-5} \text{ s}^{-1}$ interval), relative humidity (white, 10% contour interval), and wave-relative wind vectors (black) at 850 hPa. Red vectors indicate measured dropsonde winds, and yellow box indicates area shown in panel (b). Red star indicates location of the pouch ‘sweet spot’ as defined in the text. Panel (b) shows analyzed meso- β radar reflectivity (color, 3 dBZ interval), absolute vertical vorticity ($20 \times 10^{-5} \text{ s}^{-1}$ contour interval, negative denoted by dashed lines), and wave-relative wind vectors at 1.5 km altitude.

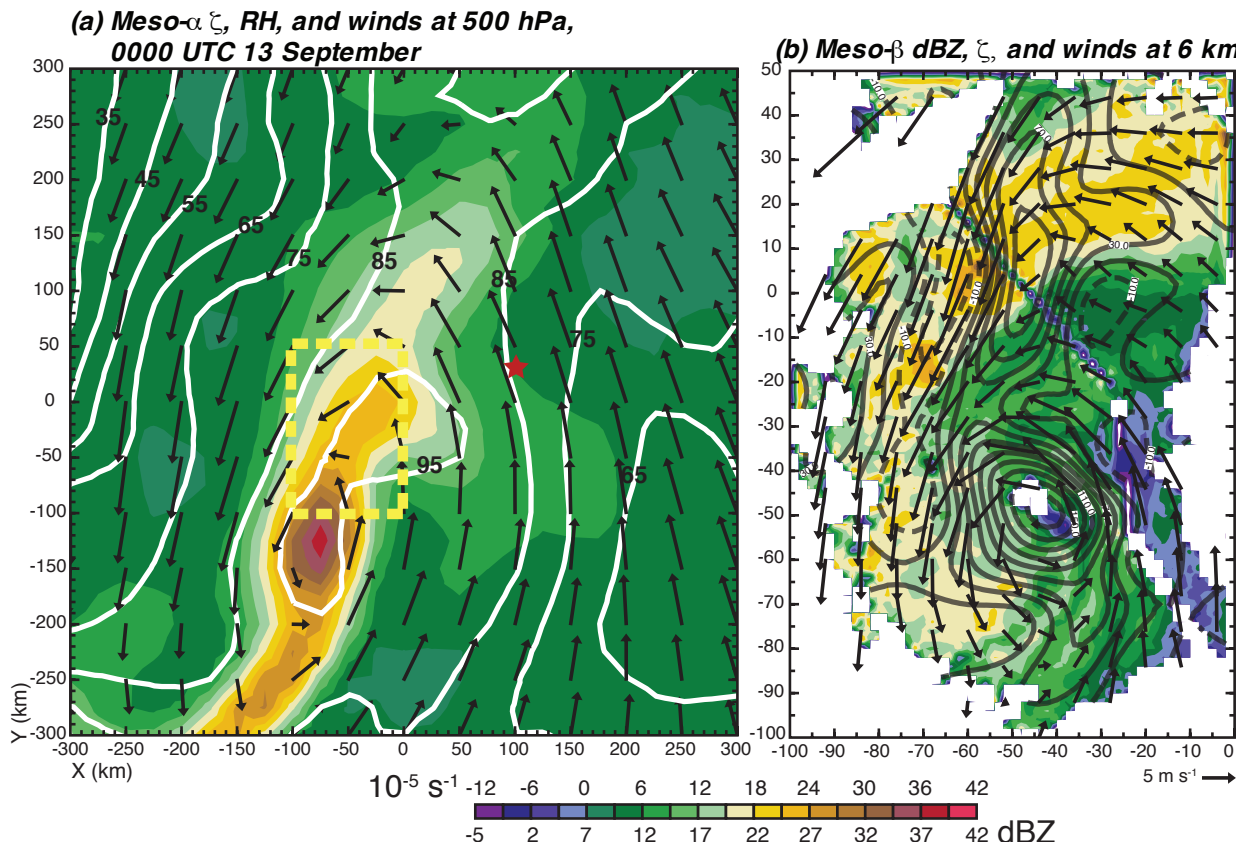


FIG. 4. Mid-level meso- α and β structure at 0000 UTC 13 September. Panels are the same as Fig. 3 except
at (a) 500 hPa and (b) 6 km altitude. Absolute vertical vorticity contours in (b) are lightened for clarity.

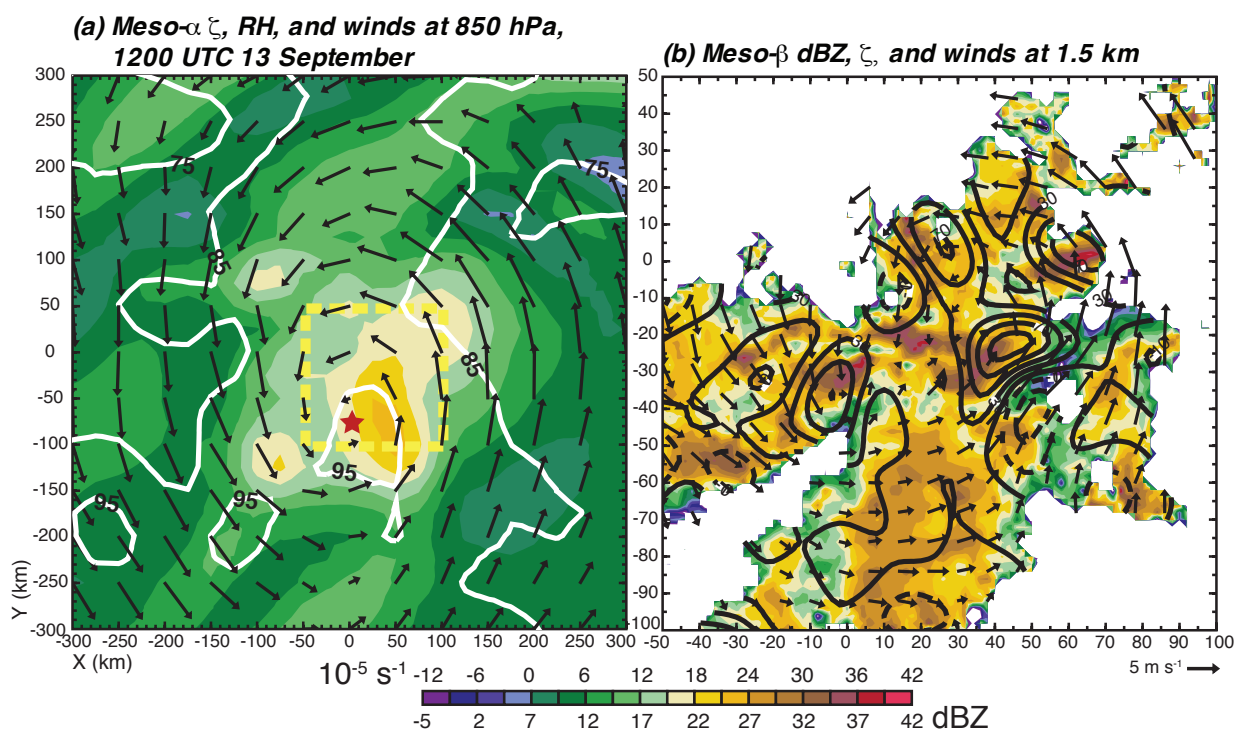
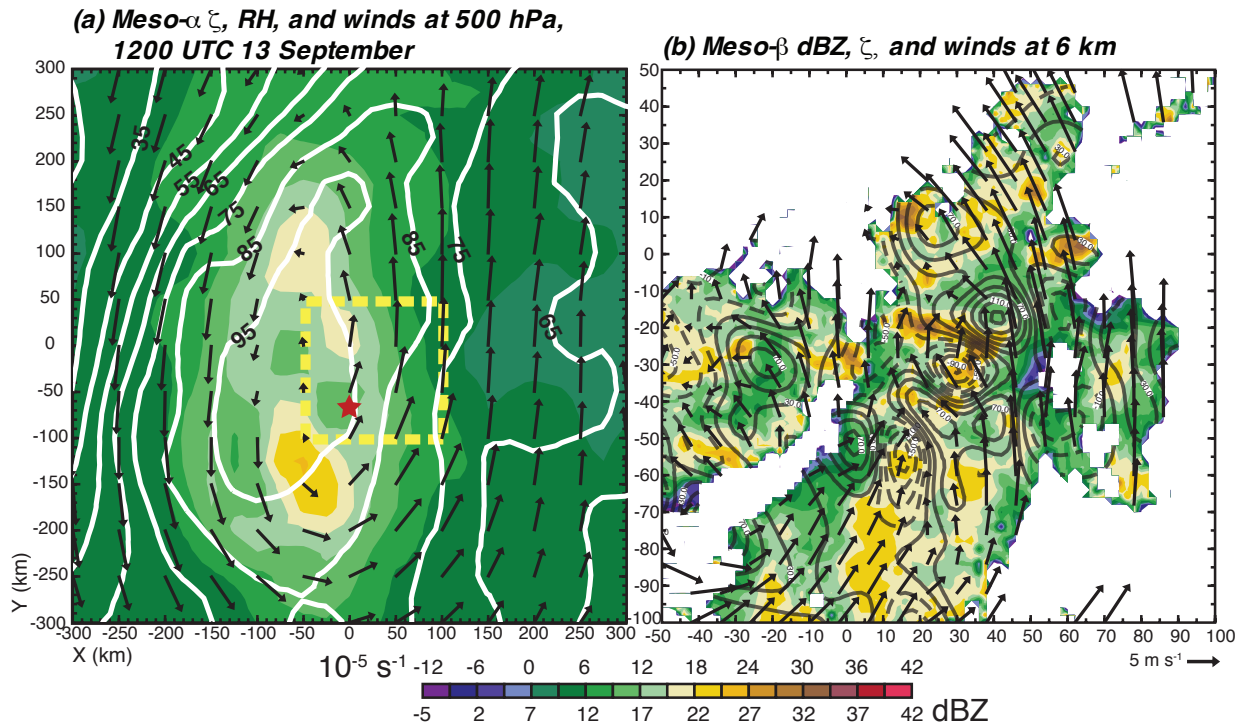


FIG. 5. Low-level meso- α and β structure at 1200 UTC 13 September. Panels are the same as Fig. 3.



954 FIG. 6. Mid-level meso- α and β structure at 1200 UTC 13 September. As in Figure 4, contours in panel (b)
955 are lightened for clarity.

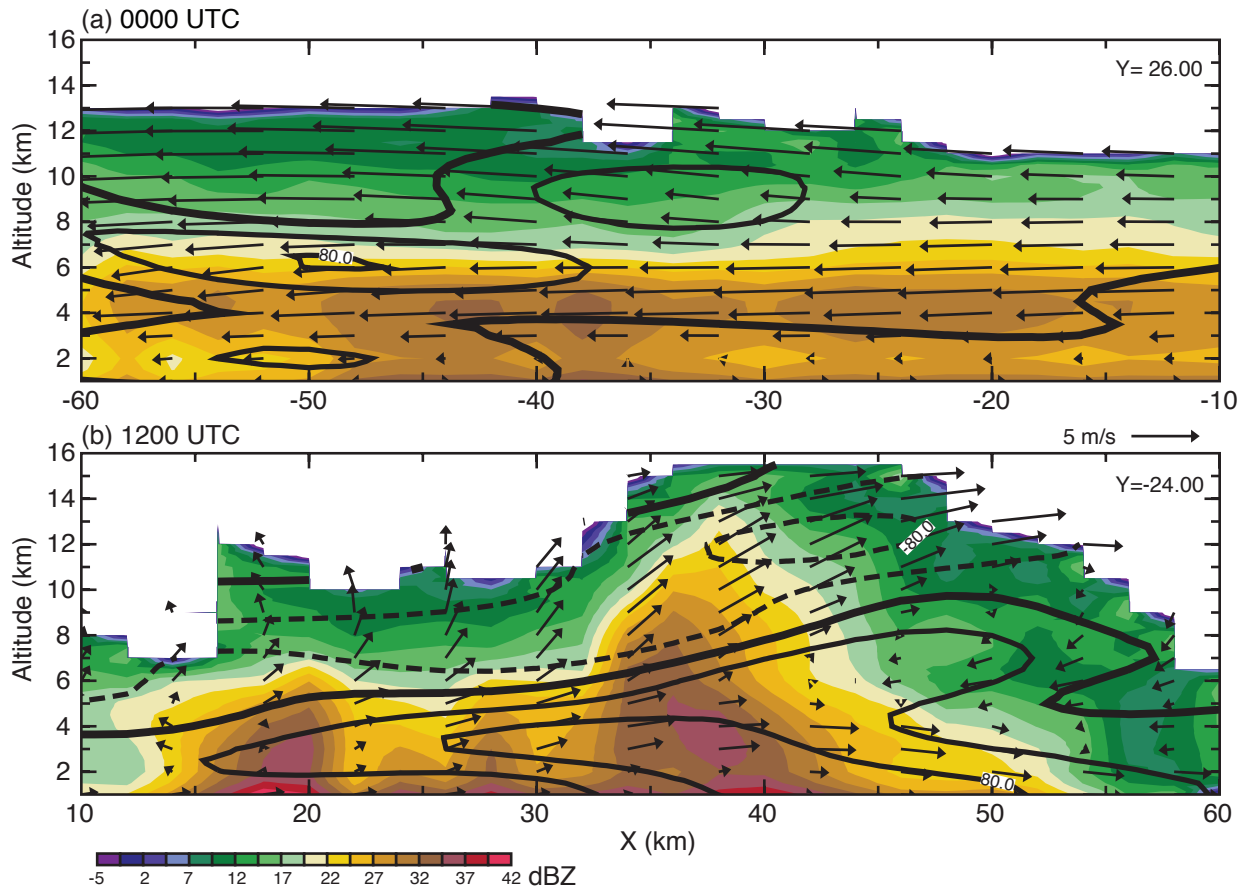


FIG. 7. Radar vertical cross-sections showing radar reflectivity (color), absolute vertical vorticity ($40 \times 10^{-5} \text{ s}^{-1}$ contour interval, negative denoted by dashed lines), and wave-relative wind vectors at (a) 0000 UTC and (b) 1200 UTC 13 September. Cross-sections are taken along (a) $Y=26 \text{ km}$ and (b) $Y = -24 \text{ km}$ in Figs. 3 and 5, respectively.

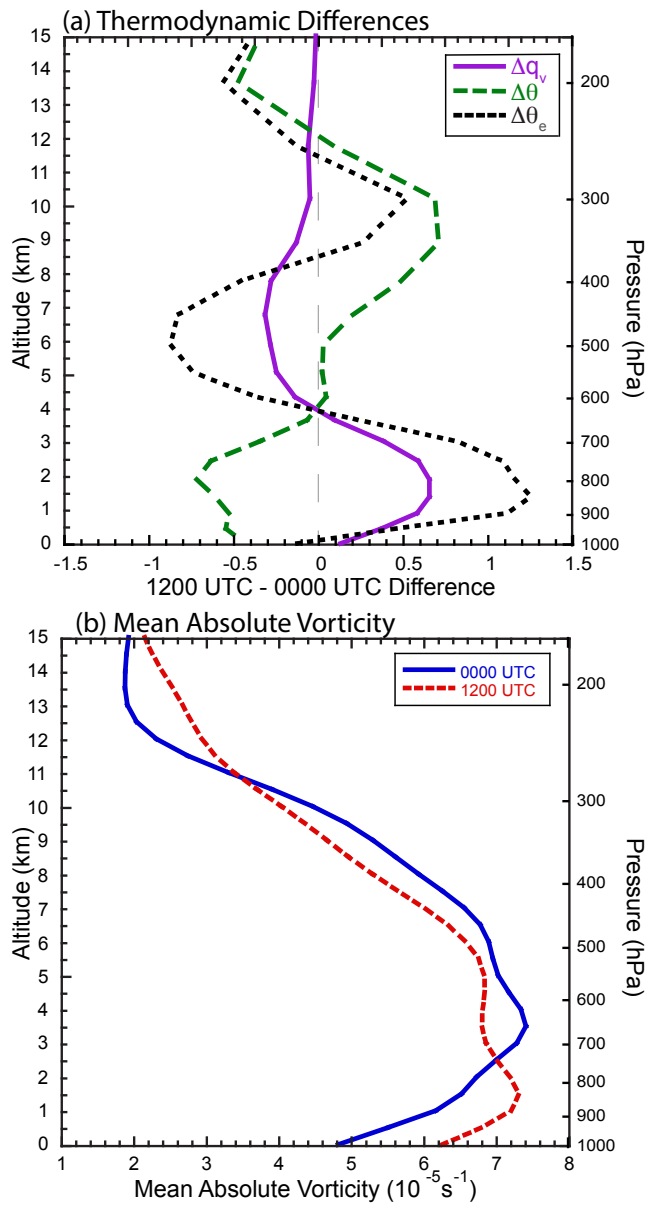


FIG. 8. Thermodynamic and vorticity differences on 600×600 km with height of meso- α averaged quantities from 0000 to 1200 UTC 13 September. Panel (a) shows difference (1200 UTC - 0000 UTC) of vapor mixing ratio (solid purple in g kg^{-1}), potential temperature (dashed green in K), and equivalent potential temperature (dotted black in K). Panel (b) shows meso- α scale averaged vorticity at 0000 UTC (solid blue) to 1200 UTC (dashed red) with height.

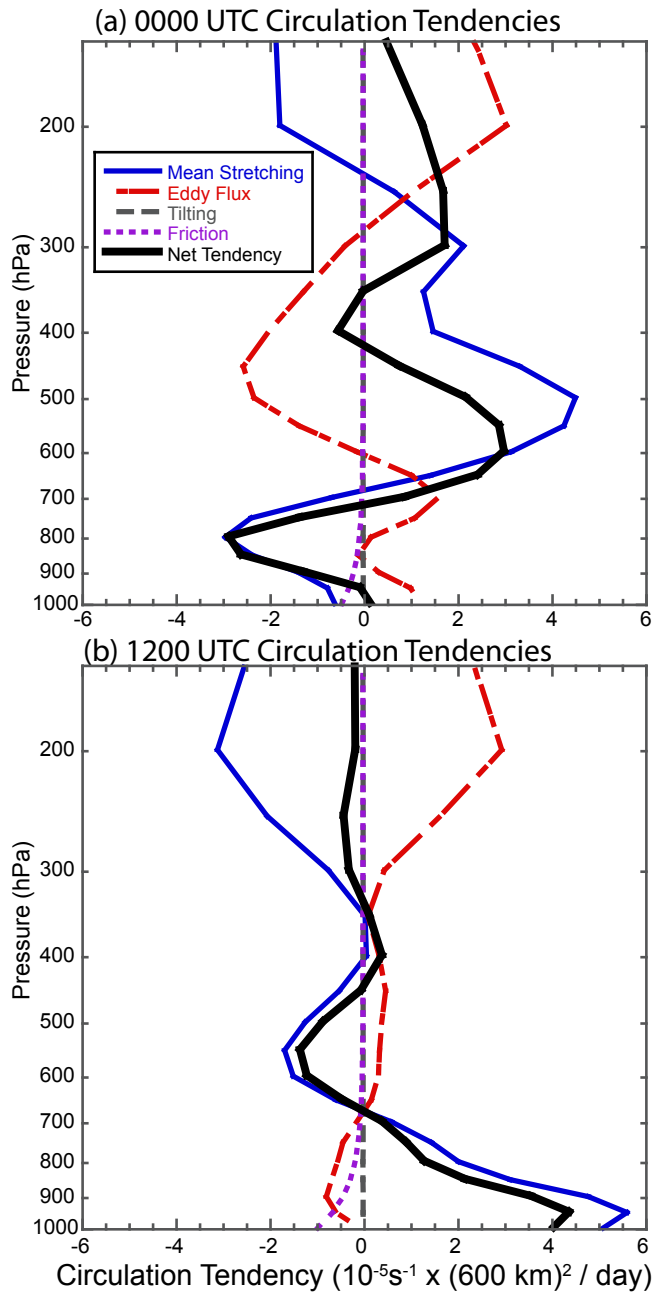


FIG. 9. Meso- α scale (600×600 km) circulation tendencies with height at (a) 0000 UTC and (b) 1200 UTC 13 September. Budget terms are mean stretching tendency (solid blue), eddy flux tendency (dash-dot red), tilting tendency (long dash gray), friction tendency (short dash purple), and net tendency calculated by summation of the component tendencies (thick solid black line).

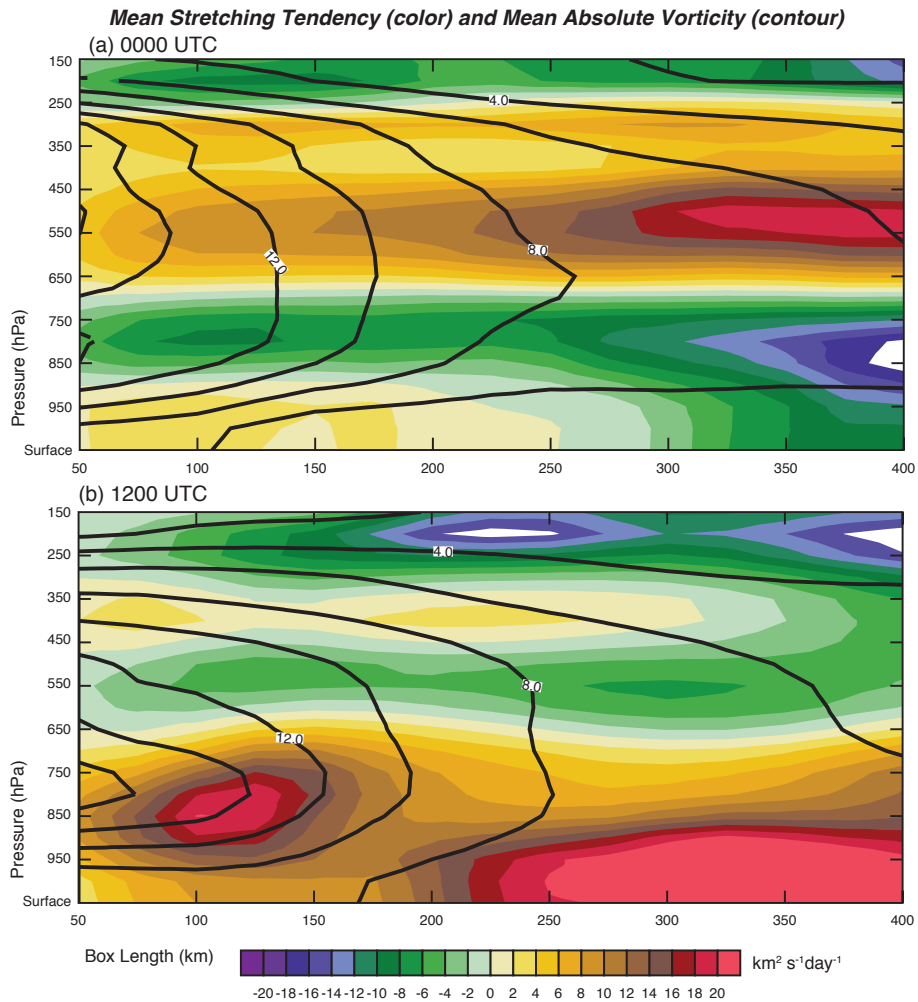


FIG. 10. Mean stretching tendency ($\text{km}^2 \text{ s}^{-1} \text{ day}^{-1}$) and absolute vorticity (10^{-5} s^{-1}) as a function of height and box length at (a) 0000 UTC and (b) 1200 UTC 13 September.

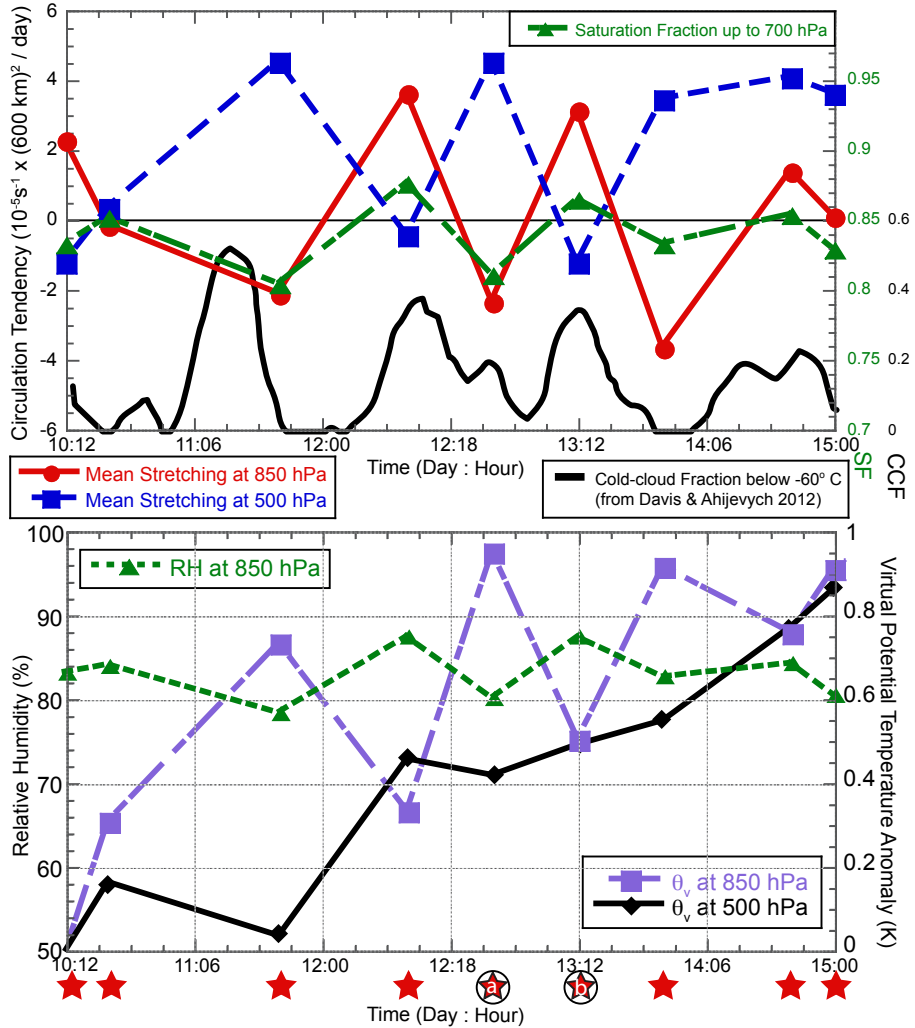


FIG. 11. Analyzed time-series of meso- α averaged quantities from initial aircraft mission to Karl's genesis.
 Panel (a) shows circulation tendency at 850 hPa (red circles) and 500 hPa (blue squares) in units of $10^{-5} \text{ s}^{-1} \times (600 \text{ km})^2 / \text{day}$. Panel (b) shows relative humidity at 850 hPa (green triangles in percent), virtual potential temperature anomaly at 850 hPa (purple squares in K), and virtual potential temperature anomaly at 500 hPa (black diamonds in K). The anomaly was calculated by removing the mean θ_v from the time series at each respective level. Red stars at bottom of figure denote mission times, with 0000 and 1200 UTC 13 September highlighted.